Modelling of Bingham and Herschel-Bulkley flows with mixed P1/P1 finite elements stabilized with Orthogonal Subgrid Scale

Elvira Moreno [*], Antonia Larese [†], Miguel Cervera [†]

[*]Departamento de Ordenación de Cuencas, Ingeniería Forestal,
Universidad de los Andes, ULA, Vía Chorros de Milla, 5001, Mérida, Venezuela

[†]International Center for Numerical Methods in Engineering (CIMNE),
Technical University of Catalonia (UPC),
Edificio C1, Campus Norte, Jordi Girona 1-3, 08034 Barcelona, Spain

July 30, 2015

Abstract

This paper presents the application of a stabilized mixed pressure/velocity finite element formulation to the solution of viscoplastic non Newtonian flows. Both Bingham and Herschel-Bulkley models are considered.

The detail of the discretization procedure is presented and the Orthogonal Subgrid Scale (OSS) stabilization technique is introduced to allow for the use of equal order interpolations in a consistent way. The matrix form of the problem is given.

A series of examples is presented to assess the accuracy of the method by comparison with the results obtained by other authors. The extrusion of a Bingham fluid and the movement of a moving and rotating cylinder are analysed in detail. The evolution of the streamlines, the yielded and unyielded regions, the drag and lift forces are presented.

These benchmark examples show the capacity of the mixed OSS formulation to reproduce the behaviour of a Bingham and Herschel-Bulkley flows with the required accuracy.

Keywords: Bingham flows, Herschel-Bulkley flows, Viscoplastic fluids, Variational multiscale stabilization, Orthogonal Subscale Stabilization, moving cylinder, extrusion.

1 Introduction

The aim of this paper is to present a continuum formulation and its correspondent discrete version for Bingham and Herschel-Bulkley confined flows, using mixed velocity/pressure linear finite elements.

Bingham and Herschel-Bulkley are viscoplastic non-Newtonian fluids characterized by the presence of a threshold stress, the yield stress. When the yield stress is exceeded the fluid flows; contrariwise, if this limit is not achieved, the fluid acts as a rigid material [37].

Bingham plastics are very common in industry. They can model the behaviour of a large number of materials, such as paints, and many products in food industry (ketchup, mayonnaise, etc). Eugene C. Bingham conceived this rheological law while studying the behaviour of paints at the beginning of XX century [10]. The Herschel-Bulkley model is a generalization of the Bingham one, and it is less known. It describes the behaviour of pastes, gels, or drilling fluids. It can be also used for simulating debris flow ([58], [75]). Both models have a strong discontinuity in their rehological behaviour due to the existence of the yield

stress, difficult to treat numerically. Different regularized formulations have been proposed to overcome this issue, Bercovier and Engelman [7], Tanner and Milthorpe [83], and Beris [8], among others. Tanner and Milthorpe were the first to propose a double viscosity model, while Beris used a Von Mises yield criterion in the unyielded zone and an ideal Bingham model in the yielded region. In 1987, Papanastasiou [67] proposed a regularization valid both for the unyielded and the yielded regions. Recently, Souza Mendes and Dutra (SMD) [40] presented a modification to the model by Papanastasou.

The movement of isothermal flows is governed by conservation of linear momentum and mass, represented by the Navier Stokes equations. In the case of non Newtonian fluids, the constitutive law has a variable viscosity whose behaviour is given by the rheological models.

Traditionally viscoplastic flows are calculated using finite elements ([1], [64], [67], [87]) but an attempt to use finite volumes were proposed by Bharti et al [9], and Tanner and Milthorpe [83] used boundary elements.

In this work a mixed velocity/pressure finite element formulation for simplicial elements is developed. This means that both velocity and pressure are interpolated piecewise linearly within the finite element mesh. This is a frequent choice in fluid dynamics because of their simplicity. On the one hand, this kind of linear elements, called $P1/P1$, present a source of instability due to the combination of the interpolation spaces of pressure and velocity [31]. The Ladyzenskaja-Babuška-Brezzi condition is not satisfied in such incompressible problem and spurious oscillations of the pressure can compromise the solution [14]. On the other hand, the convective term presents another source of instability for convection-dominated problems. The use of a proper stabilization technique is therefore needed to ensure stability and convergence of the solution.

Nowadays the most effective stabilization techniques are based on the concept of *sub-scales*. These were first introduced by Hughes [46], who proposed an Algebraic Sub-Grid Scale (ASGS) technique for the stabilization of a scalar diffusion-reaction equation. Codina generalized the approach for multidimensional systems [32]. The idea is to split the unknown in a part that can be solved by the finite element approximation plus an unresolvable scale (i.e. the sub-scale) that can not be captured by the finite element discretization. The sub-scale is approximated in a consistent residual fashion so that its variational stabilizing effect is captured. More recently, Codina proposed to use a space orthogonal to the finite element space for the subscale, introducing the Orthogonal Subgrid Scale (OSS) stabilization technique ([33], [34]). The main advantage of OSS is that it guarantees minimal numerical dissipation on the discrete solution, because it adds nothing to those components of the residual already belonging to the FE subspace. This maximizes accuracy for a given mesh, an issue always important and no less in non linear problems.

OSS has been successfully applied to the Stokes problem, to the convection-diffusion-reaction equations and to the Navier-Stokes equations. Nowadays it is used in a wide range of different problems in fluid dynamics ([32], [33], [36], [50], [51], [52], [70], [77]) and solid mechanics ([18], [19], [20], [21], [22], [23], [29], [30]). Castillo and Codina presented a three fields formulation for visco-elastic [17], power law and Carreau-Yasuda [16] fluids comparing ASGS and OSS. In the present work the OSS stabilization technique is applied to the Navier-Stokes equations to model Bingham and Hershel-Bulkley flows.

The structure of the paper is as follow. First, both the Bingham and the Herschel-Bulkley models are presented. An overview of the regularizations proposed in the literature is given. The Navier Stokes equations for a non Newtonian fluid are presented in their strong form. The corresponding discrete model is presented and the stabilization using Orthogonal Subgrid Scales (OSS) is explained in detail. The matrix form of the problem is given. Secondly, the Bingham model is applied to two well known problems: an extrusion process and a cylinder moving in a Bingham fluid confined between two parallel planes. Then, a cylinder moving in an Herschel-Bulkley fluid is modeled in two different scenarios: a cylinder moving with constant velocity and a cylinder moving and rotating around its axis. In all the cases the solution is compared with available results from other authors. Finally, some conclusions on the performance of the proposed formulation are given.

2 Viscoplastic fluids

For an incompressible fluid, the stress tensor $\boldsymbol{\sigma}$ is split as

$$\boldsymbol{\sigma} = -p\mathbf{I} + \boldsymbol{\tau} \tag{1}$$

where p is the pressure, which mutiplied by the identity matrix ($\mathbf{I}$) represents the volumetric part of the stress tensor, and $\boldsymbol{\tau}$ is the deviatoric part of the same. In a fluid, this latter is related to the rate of strain tensor $\boldsymbol{\varepsilon}$ through the viscosity μ

$$\boldsymbol{\tau} = 2\,\mu\,\boldsymbol{\varepsilon}(\mathbf{u}) = 2\,\mu\,\nabla^s\mathbf{u} \tag{2}$$

where $\mathbf{u}$ is the velocity and $\nabla^s\mathbf{u} = 1/2\left(\nabla\mathbf{u} + \nabla\mathbf{u}^T\right)$ is the symmetric part of the velocity gradient. Note that for incompressible materials, $\nabla\cdot\mathbf{u} = 0$, and the rate of strain tensor, $\boldsymbol{\varepsilon}$, is deviatoric. The kinematic viscosity μ is constant for Newtonian fluids ($\mu = \mu_0$, being μ_0 the Newtonian viscosity), but it varies in function of the velocity for non-Newtonian fluids ($\mu = \mu(\boldsymbol{\varepsilon}(\mathbf{u}))$). In this case, viscosity cannot be considered as a property of the material, as it is dependent on the deformation process. The different definitions of $\mu(\boldsymbol{\varepsilon}(\boldsymbol{u}))$ define the different families of non-Newtonian fluids ([11], [27]).

In the present work, viscoplastic fluids are considered. These are characterized by the existence of a threshold stress, the yield stress, which must be exceeded for the fluid to deform. For lower values of stress the viscoplastic fluids are completely rigid or can show some sort of elasticity. Once the yield stress is reached and exceeded, viscoplastic fluids may exhibit a Newtonian-like behavior with constant viscosity (*Bingham plastics fluids*) or with rate dependent viscosity (*Herschel-Bulkley fluids* among others).

Let us introduce, for later use, the *equivalent strain rate* $\dot{\gamma}$ and the *equivalent deviatoric stress* τ in terms of the second invariants of the rate of strain tensor ($\boldsymbol{\varepsilon}$) and of the deviatoric part of the stress tensor ($\boldsymbol{\tau}$), respectively:

$$\dot{\gamma} = (2\boldsymbol{\varepsilon} : \boldsymbol{\varepsilon})^{\frac{1}{2}} \qquad\qquad \tau = \left(\frac{1}{2}\boldsymbol{\tau} : \boldsymbol{\tau}\right)^{\frac{1}{2}} \tag{3}$$

2.1 Bingham Fluid

In 1919 Eugene C. Bingham, studying the behaviousr of paints, discovered that their deformation was almost absent till reaching a threshold yield stress. After exceeding this stress limit the paints followed a Newtonian behavior. Since a wide range of materials have been identified to have a yield threshold [67], this model was studied by many authors [65], [71], [74]. Bird [12] was the first to give a list of several Bingham plastics, most of these present in the food or chemical industries (e.g., slurries, pastes, nails, or food substances like margarine, ketchup, mayonnaise and others).

In the Bingham model the rate of strain is given by

$$\dot{\gamma} = \frac{1}{\mu_0}\left(\tau - \tau_y\right) \qquad \text{if } \tau \geq \tau_y \tag{4a}$$

$$\dot{\gamma} = 0 \qquad \text{if } \tau < \tau_y \tag{4b}$$

where μ_0 is the plastic viscosity. Considering that $\tau = \mu(\dot{\gamma})\,\dot{\gamma}$, Eq. (4a) can also be written as

$$\mu(\dot{\gamma}) = \mu_0 + \frac{\tau_y}{\dot{\gamma}} \qquad \text{if } \tau \geq \tau_y \tag{5}$$

Therefore, the deviatoric stress tensor for a Bingham plastic is defined as

$$\boldsymbol{\tau} = \left(\mu_0 + \frac{\tau_y}{\dot{\gamma}}\right)\boldsymbol{\varepsilon}(\boldsymbol{u}) \qquad \text{if } \tau \geq \tau_y \tag{6a}$$

$$\dot{\gamma} = 0 \qquad \text{if } \tau < \tau_y \tag{6b}$$

When the rate of deformation tends to zero this ideal rheological model presents a singularity and the viscosity tends to infinity ($\mu \to \infty$ as $\dot{\gamma} \to 0$). This aspect is a serious inconvenient when treating the model numerically ([11], [67], [68]). For this reason, many authors have proposed regularized versions of the Bingham model, such as the double viscosity Tanner and Milthrope model [83], the widely used Papanastasiou regularized model [67], or the Souza Mendes and Dutra (SMD) model [40]. Tanner and Milthrope substitute the rigid behaviour of the fluid with a linear dependency of the deviatoric stress by the rate of strain, introducing a fictitious viscosity when the deviatoric stress is lower than a critical strain rate. Papanastasiou introduces an exponential regularization of the viscosity

$$\mu\left(\dot{\gamma}\right) = \mu_0 + \frac{\tau_y}{\dot{\gamma}}\left(1 - e^{-m\dot{\gamma}}\right) \tag{7}$$

where m is a regularization parameter, so that $\mu = \mu_0 + \tau_y\, m$ as $\dot{\gamma} \to 0$.

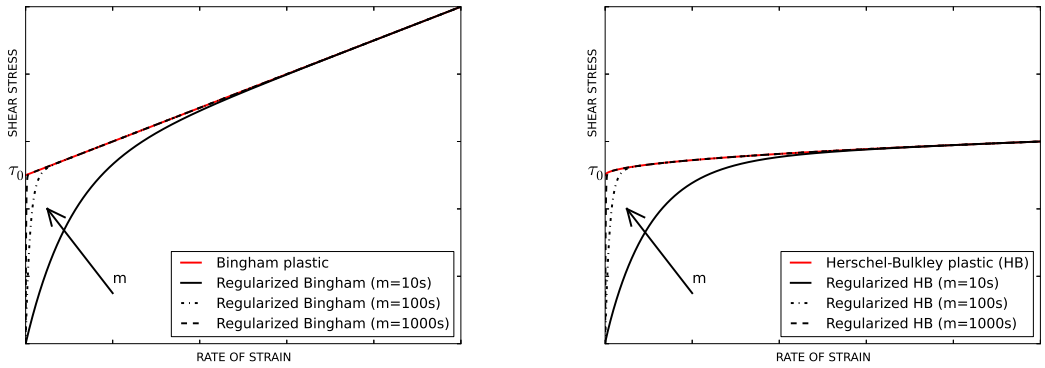

(a) Bingham model

(b) Herschel-Bulkley model

Figure 1: Bingham and Herschel-Bulkley models (red line) compared with the regularized model (black lines) for different values of m

Figure 1(a) shows the comparison between the Bingham model of Eq. (6) and the regularized one of Eq. (7). The main advantage of this approach is that the Bingham model can be defined with one equation only with full regularity. This is the regularization used in this work. The SMD can be seen as a generalization of the previous model: the exponential regularization is applied to both the terms of Eq. (5) and the regularization parameter m is substituted with a rheological parameter.

2.2 Herschel-Bulkley Fluid

The Herschel-Bulkley model [43] combines the existence of a yield stress with a power law model for the viscosity

$$\mu(\dot{\gamma}) = k\dot{\gamma}^{n-1} + \frac{\tau_y}{\dot{\gamma}} \qquad \text{if } \tau \geq \tau_y \tag{8a}$$

$$\dot{\gamma} = 0 \qquad \text{if } \tau < \tau_y \tag{8b}$$

where k is the consistency parameter and n is the flow index. Also in this case the yield stress needs to be overcome for the material to flow. When the yield stress is exceeded, the material flows with a non linear relation between stress and rate of strain as in a pseudoplastic fluid, if $n > 1$, or a dilatant one, if $n < 1$. If $n = 1$ the Bingham model is recovered, and the consistency index is equal to the plastic viscosity ($k = \mu_0$). If the yield stress is zero ($\tau_y = 0$) the Ostwald-de Waele power law fluid is recovered.

The deviatoric stress tensor is therefore

$$\boldsymbol{\tau} = 2\left(k\dot{\gamma}^{n-1} + \frac{\tau_y}{\dot{\gamma}}\right)\boldsymbol{\varepsilon}(\boldsymbol{u}) \qquad \text{if } \tau \geq \tau_y \tag{9a}$$

$$\dot{\gamma} = 0 \qquad \text{if } \tau < \tau_y \tag{9b}$$

The Herschel-Bulkley model also presents the singularity due to the perfectly rigid behaviour below the yield stress. The regularizations proposed to overcome the problem are similar to those introduced in Section 2.1. Tanner and Milthorpe proposed a double viscosity model in function of a critical strain rate to describe the elastic behavior for low strain rates [83]. Papanastasiou [67] introduced a regularization of the viscosity

$$\mu\left(\dot{\gamma}\right) = k\,\dot{\gamma}^{n-1} + \frac{\tau_y}{\dot{\gamma}}\left(1 - e^{-m\dot{\gamma}}\right) \tag{10}$$

When the rate of strain tends to zero ($\dot{\gamma} \to 0$) the viscosity depends on the flow parameter n: if $n > 1$, the $\lim_{\dot{\gamma}\to 0}\mu(\dot{\gamma}) = m\tau_y$ and, if $n = 1$, the $\lim_{\dot{\gamma}\to 0}\mu(\dot{\gamma}) = \mu + m\tau_y$; but if $n < 1$, the $\lim_{\dot{\gamma}\to 0}\mu(\dot{\gamma}) = \infty$. This means that for pseudoplastic fluids the viscosity is unbounded and a truncation procedure is needed.

Figure 1(b) shows the comparison between the Herschel-Bulkley model of Eq. 9 and the regularized one of Eq. 10.

The regularization proposed by Souza-Mendez-Dutra solves this drawback applying the regularization to all the terms of the viscosity so that $\lim_{\dot{\gamma}\to 0}\mu(\dot{\gamma}) = m\tau_y$ for any value of n [40].

The regularization proposed by Papanastasiou is the one used in the current work.

3 Governing equations

The problem of incompressible isothermal fluid is defined by the Navier-Stokes governing equation.

$$\rho\left(\partial_t\mathbf{u} + \mathbf{u}\cdot\nabla\mathbf{u}\right) - \nabla\cdot\boldsymbol{\sigma} = \mathbf{f} \qquad \text{in } \Omega,\ t \in [0,T] \tag{11a}$$

$$\nabla\cdot\mathbf{u} = 0 \qquad \text{in } \Omega,\ t \in [0,T] \tag{11b}$$

where $\Omega \subset \mathbb{R}^d$ (d is the space dimension) is the domain in a time interval $[0,T]$, ρ is the density of the fluid, and $\mathbf{f}$ are the volumetric forces.

The non-Newtonian stress tensor $\boldsymbol{\sigma}$ is defined according to Eqs. (1) and (2) and, therefore, $\nabla\cdot\boldsymbol{\sigma} = -\nabla p + \nabla\cdot\boldsymbol{\tau}$. If the regularized Bingham or Harshel-Bulkley model are used then

$$\boldsymbol{\tau} = 2\mu(\dot{\gamma})\boldsymbol{\varepsilon}(\mathbf{u}) \tag{12}$$

with $\mu(\dot{\gamma})$ defined by Eq. (7) or Eq. (10), respectively. The problem is fully defined with the boundary conditions:

$$\mathbf{u}(\mathbf{x},t) = \overline{\mathbf{u}}(\mathbf{x},t) \qquad \text{on} \quad \partial\Omega_D, \quad t \in [0,T], \tag{13a}$$

$$\mathbf{n}\cdot\boldsymbol{\sigma}(\mathbf{x},t) = \mathbf{t}(\mathbf{x},t) \qquad \text{on} \quad \partial\Omega_N, \quad t \in [0,T], \tag{13b}$$

where $\partial\Omega_D$ and $\partial\Omega_N$ are the Dirichlet and the Neumann boundaries, respectively ($\partial\Omega_D \cap \partial\Omega_N = \emptyset$, $\partial\Omega_D \cup \partial\Omega_N = \partial\Omega$).

Steady-state flows are modelled by dropping the time derivative term in Eq. (11a). Likewise, the convective term can be neglected for low Reynolds numbers, as it is usually the case for viscoplastic fluids.

4 Discrete model

The governing equations (Eqs. (11)) are solved using mixed stabilised linear/linear finite elements for the spatial discretization.

The weak form of the problem is obtained using a Galerkin technique and the non linear terms of the momentum equation (i.e. the convective and viscous terms of Eq. (11a)) are linearized using a secant Picard method. The velocity $\mathbf{u}$ needs to belong to the velocity space $\mathcal{V} \in [\mathbf{H}^1(\Omega)]^d$ of vector functions whose components and their first derivatives are square-integrable and the pressure p belongs to the pressure space $\mathcal{Q} \in \mathbf{L}_2$ of square-integrable functions.

Let $\mathcal{V}_h \subset \mathcal{V}$ be a finite element space to approximate $\mathcal{V}$, and $\mathcal{Q}_h \subset \mathcal{Q}$ a finite element approximation to $\mathcal{Q}$. Let $\Omega \subset \mathbb{R}^d$ be the domain in a time interval $[0, T]$, and Ω^e the elemental domain such that $\bigcup \Omega^e = \Omega$, with $e = 1, 2, ..., n_{el}$ where n_{el} is the number of elements.

Therefore, the standard Galerkin discrete problem is finding $\mathbf{u}_h \in \mathcal{V}_h$ and $p_h \in \mathcal{Q}_h$ such that

$$\int_\Omega \left[\rho \partial_t \mathbf{u}_h \cdot \mathbf{v}_h + \rho \left(\mathbf{u}_h \cdot \nabla \mathbf{u}_h\right) \cdot \mathbf{v}_h + 2\mu(\dot{\gamma}) \nabla^s \mathbf{u}_h : \nabla^s \mathbf{v}_h - p_h \nabla \cdot \mathbf{v}_h - \mathbf{f}_h \cdot \mathbf{v}_h\right] d\Omega = 0 \quad \forall \mathbf{v}_h \in \mathcal{V}_h \tag{14a}$$

$$\int_\Omega \left[q_h \nabla \cdot \mathbf{u}_h\right] d\Omega = 0 \quad \forall q_h \in \mathcal{Q}_h \tag{14b}$$

$\mathbf{w}_h$ and q_h are the velocity and the pressure weight functions belonging to velocity and pressure spaces, respectively, and some of the terms have been integrated by parts.

4.1 Stabilized model

In this work, low-order simplicial elements are used with the same linear interpolation for the velocity and pressure fields. This implies that the Ladyzenskaja-Babuška-Brezzi condition, also called the *inf-sup condition*, is not respected and a stabilization technique is needed to overcome the instability of the pressure that may compromise the solution.

The stabilization employed is based on the subgrid scale approach proposed by Hughes ([15], [45], [47]). This proposes to split the velocity field ($\mathbf{u}$) into a part that can be represented by the finite element mesh ($\mathbf{u}_h$) and another part that accounts for the unresolvable scale ($\overline{\mathbf{u}}$), that is, for the variation of the velocity that cannot be captured by the finite element mesh. This corresponds to a splitting of the space $\mathcal{V}$ into the space of the finite elements ($\mathcal{V}_h$) and the subgrid space ($\overline{\mathcal{V}}$), so that $\mathcal{V} = \mathcal{V}_h \oplus \overline{\mathcal{V}}$.

The sub-scale $\overline{\mathbf{u}}$ is approximated from the residual of the momentum equation and it is evaluated inside each element, assuming the sub-scale to vanish on the boundary of each element. Different approximations of the sub-scale $\overline{\mathbf{u}}$ define different stabilization techniques.

In the present work, the Orthogonal Sub-grid Scale stabilization technique is used. This method was proposed by Codina ([33], [34], [35]) as a modification of the Algebraic Sub-Grid Scale (ASGS). In ASGS the sub-scale is taken proportional to the residual ($\mathbf{R}_h = -\rho \left(\mathbf{u}_h \cdot \nabla \mathbf{u}_h\right) + \nabla \cdot \boldsymbol{\sigma}_h + \mathbf{f}_h$) of the momentum equation, so that $\overline{\mathbf{u}} = -\tau_1 \mathbf{R}_h$, where τ_1 is a stabilization parameter. An application of ASGS to non Newtonian fluid models can be found in [51] and [78]. Contrariwise, in the OSS the sub-scale is taken proportional to the orthogonal projection of the residual onto the finite element space

$$\overline{\mathbf{u}} = -\tau_1 P_h^\perp \left(\mathbf{R}_h\right) = -\tau_1 \left(\mathbf{R}_h - P_h \left(\mathbf{R}_h\right)\right) \tag{15}$$

where $P_h(\bullet)$ is the projection on the finite element space and $P_h^\perp(\bullet) = I(\bullet) - P_h(\bullet)$ is the orthogonal projection.

Residual based stabilization techniques such as ASGS and OSS do not introduce any consistency error, as the exact solution annuls the added terms, so that the stabilized model converges to the solution of the problem in continuum format. Also, if designed properly, the convergence rate is not altered; that is, the subscale terms must be appropriately dependent on the mesh size.

Constructing the subscale in the subspace orthogonal to the finite element subspace has several advantages over the many other possibilities. The main one is that it guarantees minimal numerical dissipation on the discrete solution, because it adds nothing to those components of the residual already belonging to the FE subspace. This maximizes accuracy for a given mesh, an issue always important and no less in non linear problems.

Additionally, in transient problems, the term corresponding to the time derivative belongs to the finite element space, and therefore, its orthogonal projection is null. This means that the mass matrix remains unaltered by the stabilization method, maintaining its structure and symmetry.

Moreover, if the residual can be split in two or more terms, e.g. if the stress tensor is split into its volumetric and deviatoric parts or if the residual includes a convective term, then the "cross products" in the stabilization terms can be neglected. This has three advantages: i) it reduces the computational stencil, (ii) more selective norms can be defined for stability control and (iii) it has proved important in problems involving singular or quasi-singular points both in linear and non-linear problems.

The part of the residual to be orthogonally projected can be appropriately selected. For instance, in incompressible problems, only the gradient of the pressure needs to be added to ensure control of the pressure, with minimal numerical dissipation. These variants of the OSS, that can be considered to belong to the family of term-by-term stabilization methods, introduce consistency errors, but they are of optimal order and the final convergence rate of the scheme is not altered.

The discretized linearized problem, stabilized with OSS is, find $\mathbf{u}_h^{n+1}$ and p_h^{n+1} such that

$$\begin{aligned}\int_\Omega \Big[& \frac{\rho}{\delta t}\left(\mathbf{u}_h^{n+1}-\mathbf{u}_h^{n}\right)\cdot\mathbf{v}_h + \rho\left(\mathbf{u}_h^{n+1}\cdot\nabla\mathbf{u}_h^{n+1,\,i}\right)\cdot\mathbf{v}_h \\ & + 2\mu(\dot{\gamma})^{n+1,\,i}\nabla^s\mathbf{u}_h^{n+1} : \nabla^s\mathbf{v}_h - p_h^{n+1}\nabla\cdot\mathbf{v}_h - \mathbf{f}_h^{n+1}\cdot\mathbf{v}_h\Big]\, d\Omega \\ & + \sum_e \int_{\Omega^e} \tau_1\rho\left(\mathbf{u}_h^{n+1}\cdot\nabla\mathbf{v}_h\right)\cdot\left[\rho\mathbf{u}_h^{n+1}\cdot\nabla\mathbf{u}_h^{n+1} + \nabla p_h^{n+1} - \mathbf{f}_h^{n+1} - \rho\mathbf{v}_h^{*}\cdot\mathbf{y}_h^{n+1}\right] d\Omega = 0 \quad \forall\mathbf{v}_h\in\mathcal{V}_h\end{aligned} \tag{16a}$$

$$\int_\Omega \left[q_h\nabla\cdot\mathbf{u}_h^{n+1}\right] d\Omega + \sum_e \int_{\Omega^e} \tau_1\nabla q_h\cdot\left[\left(\rho\mathbf{u}_h^{n+1}\cdot\nabla\mathbf{u}_h^{n+1} + \nabla p_h^{n+1} - \mathbf{f}_h^{n+1}\right) - \rho\mathbf{v}_h^{*}\cdot\mathbf{y}_h^{n+1}\right] d\Omega = 0 \quad \forall q_h\in\mathcal{Q}_h \tag{16b}$$

where $\mathbf{y_h}$ is the nodal projection defined as

$$\mathbf{y_h}^{n+1} = P_h\left(\mathbf{u}_h^{n+1}\cdot\nabla\mathbf{u}_h^{n+1} + \frac{1}{\rho}\left(\nabla p_h^{n+1} - \mathbf{f}_h^{n+1}\right)\right) \tag{17}$$

In compact notation, the projection of Eq. (17) is the solution of

$$\left(\mathbf{y_h}^{n+1}, \mathbf{v}_h^{*}\right) = \left(\mathbf{u}_h^{n+1}\cdot\nabla\mathbf{u}_h^{n+1} + \frac{1}{\rho}\left(\nabla p_h^{n+1} - \mathbf{f}_h^{n+1}\right), \mathbf{v}_h^{*}\right) \tag{18}$$

for all $\mathbf{v}_h^{*}\in\mathbf{V}_h^{*}$, being $\mathbf{V}_h^{*}$ equal to $\mathbf{V}_h$ extended with the vectors of continuous functions associated to the boundary nodes.

The stabilization parameter τ_1 in Eqs. (16a) and (16b) is defined so to obtain a stable numerical scheme and an optimal velocity of convergence. Consequently, τ_1 is calculated for each element as [34]

$$\tau_1 = \left[c_1\frac{\mu}{h_e^2} + c_2\frac{\rho|\mathbf{u}^e|}{h_e}\right]^{-1} \tag{19}$$

where h is the characteristic length of the e-th element and $|\mathbf{u}^e|$ is the norm of velocity in the element. c_1 and c_2 are two coefficients that in the present work are chosen as $c_1 = 4$ and $c_2 = 2$ [34].

5 Matrix form

The solution system (16) is rewritten in matrix form as

$$\mathbf{M}\frac{1}{\delta t}\mathbf{U}^{n+1} + \mathbf{K}(\mathbf{U}^{n+1})\mathbf{U}^{n+1} + \mathbf{G}\mathbf{P}^{n+1} + \mathbf{S}_u(\tau_1;\mathbf{U}^{n+1})\mathbf{U}^{n+1} - \mathbf{S}_y(\tau_1;\mathbf{U}^{n+1})\mathbf{Y}^{n+1} = \mathbf{F}^{n+1} \tag{20a}$$

$$\mathbf{D}\mathbf{U}^{n+1} + \mathbf{S}_p(\tau_1)\mathbf{P}^{n+1} - \mathbf{S}_z(\mathbf{U}^{n+1})\mathbf{Y}^{n+1} = 0 \tag{20b}$$

$$\mathbf{C}(\mathbf{U}^{n+1})\mathbf{U}^{n+1} + \mathbf{G}_\pi\mathbf{P}^{n+1} = 0 \tag{20c}$$

where $\mathbf{U}$ and $\mathbf{P}$ are the vectors of nodal velocities and pressures, respectively, $\mathbf{Y}$ is the vector of nodal projections and $\mathbf{F}$ is the vector of nodal forces.

Finally, the matrix operators of Eqs. (20) are defined as

$$\mathbf{M}_{ij}^{ab} = \left(N^a, \rho N^b\right)\delta_{ij} \tag{21a}$$

$$\mathbf{K}\left(\mathbf{U}^{n+1}\right)_{ij}^{ab} = \left(N^a, \rho\mathbf{u}_h^{n+1}\cdot\nabla N^b\right)\delta_{ij} + \left(\nabla N^a, 2\mu\nabla^s N^b\right)\delta_{ij} \tag{21b}$$

$$\mathbf{G}_i^{ab} = \left(N^a, \partial_i N^b\right) \tag{21c}$$

$$\mathbf{F}_i^a = \left(N^a, \mathbf{f}_i\right) \tag{21d}$$

$$\mathbf{D}_j^{ab} = \left(N^a, \partial_j N^b\right) \tag{21e}$$

$$\mathbf{C}\left(\mathbf{U}^{n+1}\right)_{ij}^{ab} = \left(N^a, \mathbf{u}_h^{n+1}\cdot\nabla N^b\right)\delta_{ij} \tag{21f}$$

$$\mathbf{G}_{\pi}{}_i^{ab} = \left(N^a, \partial_i N^b/\rho\right) \tag{21g}$$

The stabilization operators of Eqs. (20) are

$$\mathbf{S}_\mathbf{u}\left(\tau_1, \mathbf{U}^{n+1}\right)_{ij}^{ab} = \left(\tau_1\mathbf{u}_h^{n+1}\cdot\nabla N^a, \rho\mathbf{u}_h^{n+1}\cdot\nabla N^b\right)\delta_{ij} \tag{22a}$$

$$\mathbf{S}_\mathbf{y}\left(\tau_1\mathbf{u}_h^{n+1}\right)_{ij}^{ab} = \left(\tau_1\mathbf{u}_h^{n+1}\cdot\nabla N^a, \rho N^b\right)\delta_{ij} \tag{22b}$$

$$\mathbf{S}_\mathbf{p}\left(\tau_1\right)^{ab} = \left(\tau_1\mathbf{u}_h^{n+1}\cdot\nabla N^a, \nabla N^b\right) \tag{22c}$$

$$\mathbf{S}_\mathbf{z}\left(\tau_1\right)_j^{ab} = \left(\tau_1\partial_j N^a, \rho N^b,\right) \tag{22d}$$

6 Numerical results: Bingham Fluids

6.1 Extrusion

6.1.1 Description of the problem

, The first example is the extrusion process of a Bingham fluid. Extrusion is widely used in several industrial processes such as metal forming, manufacturing, food production, etc. Real applications are usually in three dimensions; nevertheless, a plane strain $2D$ analysis provides very useful information on the evolution of the plastic region and gives an estimation of the forces required in the process.

The *slip-lines theory* was first introduced by Prandtl at the beginning of the XX century [72]. This methodology was originally used in plane strain problems to estimate the stress field and the related velocity

field in perfect plastic materials with the Von Mises (or Tresca) yield criterion. The approach was generalized by Mandel [56], who introduced other yield criteria and analyzed the plane stress case [55].

The slip lines are tangent to the direction of the maximum tangential stress and are the trajectories of the maximum shear stress. In plain strain, the plastic flow coincides with the maximum shear stress direction. Therefore, rigid-plastic material "*slips*" in the direction of the maximum shear stress lines.

In 1948, Hill [44] used the slip line theory to analytically solve the problem of direct frictionless extrusion in a die with a 50% reduction of its section. In 1961, Alexander [3] demonstrated that if the reduction of the die section is of 2/3, there exists a part of the yielded region (the area ABDC in Figure 2) in which the average pressure coincides with the extrusion pressure p

$$p = \frac{4}{3}\left(1 + \frac{\pi}{2}\right)\tau_y \tag{23}$$

where τ_y is the yield stress.

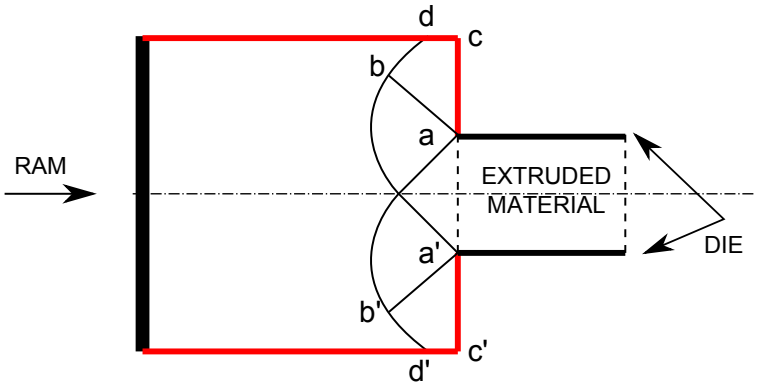

Figure 2: Extrusion of a Bingham fluid. Slip lines according to Alexander [3]

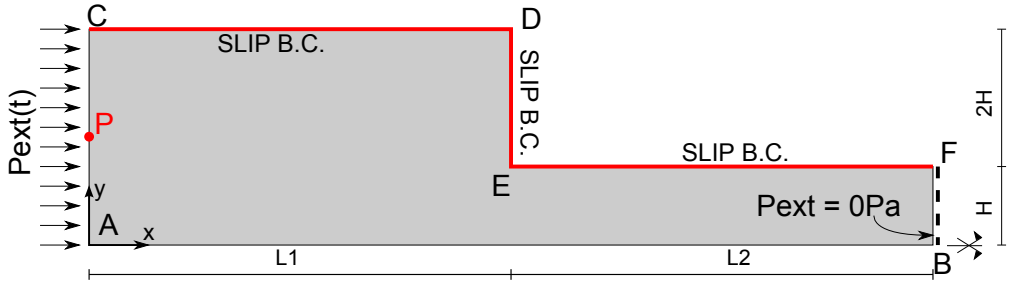

Figure 3: Extrusion of a Bingham fluid. Geometry and boundary conditions

The extrusion process can be numerically simulated using either a Lagrangian plastic flow or an elasto-plastic solid. In the first case, the elastic deformation is neglected and the material follows the Von Mises yield criterion and an associated flow rule. Zienkiewicz [87] and Oñate [66] applied this approach to analyze the plain stress problem without hardening using a Lagrangian mesh moving with the material. In the second case, the elastic strains are considered, which complicates the problem introducing both geometrical and material non linearities. In 1984, Lee [53] published one of the first examples of an extrusion problem using a large deformation elasto-plastic approach. He used an updated Lagrangian technique and the Von Mises yield criterion with hardening.

A widely used alternative is to use an Eulerian viscoplastic flow and a Von Mises yield criterion ([39], [42], [49], [68]). In this case, the material follows a rigid-plastic law with a very low plastic viscosity (almost

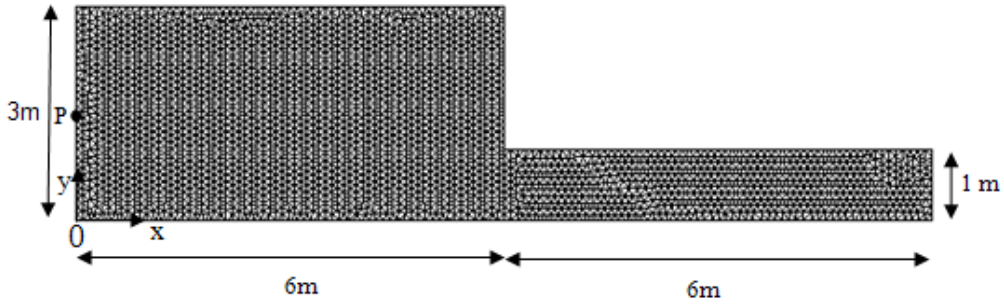

Figure 4: Extrusion of a Bingham fluid. Mesh used in the calculation: 2821 nodes and 5340 linear triangular elements

perfect plasticity). Once the yield stress is reached, a high localization of the strain rate occurs. This can be identified with the slip lines of Prandtl theory. This is the formulation used in this work with the objective of identifying the yielded and unyielded regions, the evolution of the stream lines and of the slip lines. The calculated pressure on the ram is compared with the analytical solution given by Eq. (23).

6.1.2 Model and results

The geometry and boundary conditions used are presented in Figure 3. A reduction of 2/3 is considered. A slip condition is imposed on the wall boundaries CDEF and C'D'E'F'. An increasing normal stress is imposed on CC'. This represents the ram pressure that increases linearly with time from $p = 0$ Pa at the initial time ($t = 0$ s) to $p = 5000$ Pa at $t = 1$ s. The vertical component of velocity is set to zero on CC'. The pressure is set to zero in point B, and the horizontal velocity is left free in point E.

A $2D$ plane strain simulation is carried on. Exploiting the symmetry of the problem, only half of the domain is discretized using 2821 nodes 5340 and linear/linear ($P1/P1$) triangular elements (see Figure 4).

The material parameters are summarized in Table 1 where the regularization coefficient employed for the Bingham model is also given.

Material properties		
Plastic viscosity	μ_0	10^{-6} Pa · s
Density	ρ	100 kg/m^3
Yield stress	τ_y	1000 Pa
Regularization		
Regularization coefficient m		1000 s

Table 1: Extrusion in a Bingham fluid. Material parameters and regularization coefficient

The example is solved as a series of steady-state problems with increasing ram pressure. Two scenarios have been taken into account: with and without the convective term in the momentum equation. Figure 5 shows the velocity evolution on point P while the pressure on the ram is increased, in comparison with the analytical solution (continuous line). At $t = 0.69$ s the flow is fully developed and the yielded regions are completely defined. The numerical pressure for yielding is $P_{num} = 3400$ Pa, while the analytical solution is $P_{an} = 3428$ Pa according to Eq. (23).

If the convection term is included in the momentum equation (black dotted line in Figure 5), it is necessary to increase the external pressure in order to overcome the inertial effects once the yield stress is achieved. This does not happen when the convective term is neglected (red dotted line in Figures 5). In this case, once the slip lines have developed, very large velocities are achieved with a very small increment of external pressure.

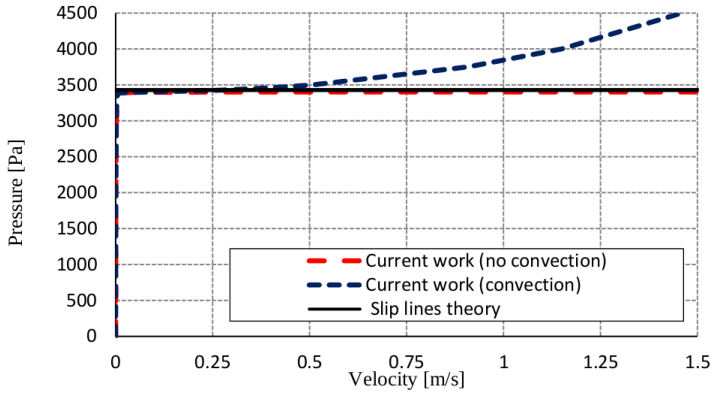

Figure 5: Extrusion of a Bingham fluid. Pressure-velocity curve in point P (see Figure 4). Comparison between the analytical solution and the numerical results

Figure 6 presents the stream lines evolution during the extrusion process. An abrupt change in the smoothness of the streamlines is observed when the slip lines appear (Figure 6(c) and 6(d)). Figure 6 also shows the yielded (dark) and un-yielded (fair) regions above and below the critical strain rate ($\dot{\gamma}_{crit} = 0.01688$ s^{-1}, correspondent to $\tau = \tau_y$).

The evolution of the velocity field is presented in Figure 7. It can be observed that while at $t = 0.6$ s almost all the domain is solid and just a very small region has reached the yield threshold, at $t = 0.678$ s the extrusion mechanism and the slip lines are fully developed. This lines coincide with the slip lines of the classical plastic theory [55].

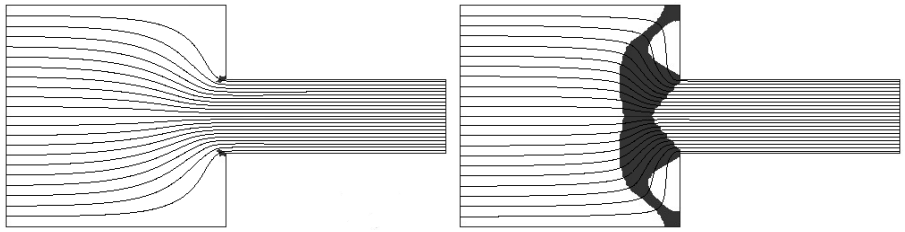

(a) $t = 0.6$ s (b) $t = 0.677$ s

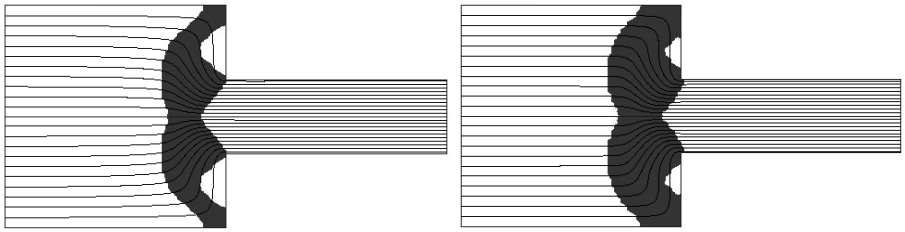

(c) $t = 0.678$ s (d) $t = 0.68$ s

Figure 6: Extrusion in a Bingham fluid. Evolution of the stream lines and of the yielded region (dark) for $\tau_y = 1000$ Pa and $\dot{\gamma}_{crit} = 0.01688$ s^{-1} at $t = 0.6$, 0.677, 0.678 and 0.68 s

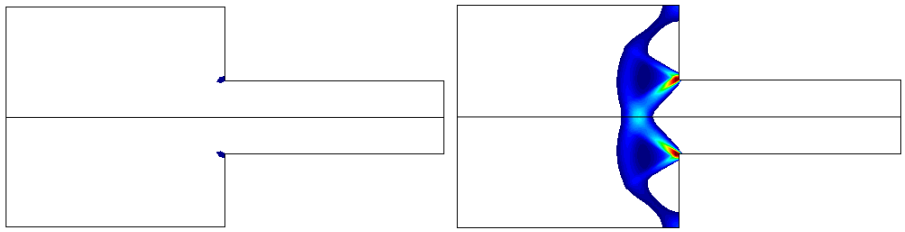

(a) $t = 0.6$ s (b) $t = 0.6$ s

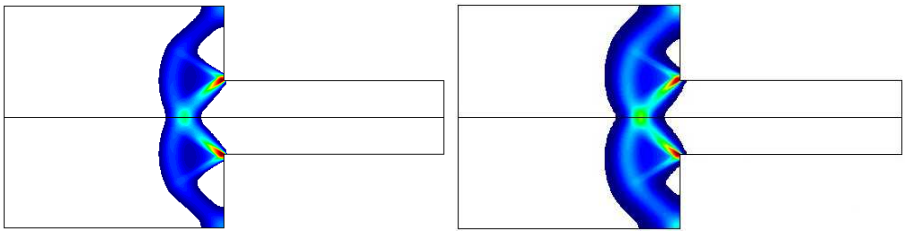

(c) $t = 0.6$ s (d) $t = 0.6\,s$

Figure 7: Extrusion in a Bingham fluid. Evolution of the velocity field for $\tau_y = 1000$ Pa and $\dot{\gamma}_{crit} = 0.01688$ s^{-1} at $t = 0.6$, 0.677, 0.678 and 0.68 s

6.2 Flow around a cylinder between two parallel planes

6.2.1 Description of the problem

The flow around a cylinder in a confined Bingham fluid is studied in this second example. The flow around an obstacle was initially studied considering a spherical object. This classical problem in computational fluid dynamics has several practical applications in different engineering fields: from segregation in food industry, to transport of mud in geotechnical engineering or aerosols in environmental engineering, etc. The geneeral problem is the suspension of large particles in a fluid with a yield threshold. The falling or settlement of the particles can only occur if the gravity force exceeds the yield limit ([24], [73], [81]).

The viscoplastic flow around an obstacle has been widely studied both numerically and experimentally ([24], [26], [41], [85]). For the specific case of Bingham plastics, many authors have proposed different solutions for the flow around a sphere subjected to gravity force between two parallel planes or in an infinite domain ([13], [54], [60], [88]). Moreover, Roquet and Sarmito [76] studied the effect of an additional pressure gradient and Slijecpčević and Perić [80] studied the movement of a sphere inside a cylinder.

Nowadays, there exists abundant literature on a sphere falling either in a pseudoplastic, viscoplastic or viscoelastic fluid for low Reynolds numbers [25]. Contrariwise, not many authors have treated the movement of a cylinder in a non-Newtonian fluid.

The aim of this example is to define the yielded zones and the hydrodynamic drag force in terms of the geometrical configuration of the parallel planes and the cylinder.

6.2.2 Adimensional forces

In this and the following examples a series of adimensional quantities will be used to present the results. These quantities are defined here.

Being x the direction of the flow and y its orthogonal direction in the plane (see Figure 8(a)), the drag force (F_D) and lift force (F_L) acting on the cylinder can be calculated as

$$F_D = lR \int_0^{2\pi} t_x \, d\theta = 4lR \int_0^{\pi/2} [\sigma_{xx} \, cos\theta + \sigma_{xy} \, sin\theta] \, d\theta \tag{24}$$

and

$$F_L = lR \int_0^{2\pi} t_y \, d\theta = 4lR \int_0^{\pi/2} [\sigma_{xy} \, cos\theta + \sigma_{yy} \, sin\theta] \, d\theta \tag{25}$$

where $R = 1$ m is the radius and $l = 1$ m is the height of the cylinder. The traction vector $\mathbf{t}^T = (t_x, \, t_y)$ is defined by the stress components in the xy plane (i.e., σ_{xx}, σ_{yy}, σ_{xy}) and of angle θ between the normal to the cylinder and the x axis as $t_x = \sigma_{xx} cos\theta + \sigma_{xy} sin\theta$ and $t_y = \sigma_{xy} cos\theta + \sigma_{yy} sin\theta$.

The adimensional drag and lift coefficients in the specific case of a Bingham fluid are

$$F_D^* = \frac{F_D}{\mu V l} \qquad ; \qquad F_L^* = \frac{F_L}{\mu V l} \tag{26}$$

An information on the relevance of the yield stress in the resistance that the flow provides to the movement of the cylinder is given by the drag coefficient $F_D^{'}$. This is by definition the ratio between the drag force and the yield stress

$$F_D^{'} = \frac{F_D}{\tau_y} \tag{27}$$

Finally, the last adimensional quantity used in the paper is the adimensional yield stress τ_y^* associated to the drag force

$$\tau_y^* = \frac{2\tau_y \pi R^2}{F_D}. \tag{28}$$

6.2.3 Model and results

The cylinder with radius $R = 1$ m is located between two infinite parallel planes. The distance between the planes is $2H$ and the center of the cylinder is at distance H from both of them. The system of reference is attached to the center of the cylinder and it is considered fixed (Figure 8(a)). The planes are moving with velocity V as well as the lateral sides of the computational domain, located sufficiently far from the cylinder. No slip is assumes on the surface of the cylinder and inertial effects are ignored ($Re \approx 0$). The flow has double symmetry, with respect both to the vertical and to the horizontal axes. For this reason, just a quarter of the domain is analyzed (see Figure 8(b)) ([8], [69]).

Figure 8(b) shows a schematic description of the boundary conditions used. A no slip condition is applied on line AB, orthogonal velocity and tangential stresses are zero on lines BC and AD. The velocity is fixed on ED and on the upper wall where the vertical component $u_y = 0$ and the horizontal one $u_x = V = 1$ m/s. Pressure is set to zero on C to determine univocally the pressure field. The length of the domain (L in Figure 8(b)) is sufficiently large to ensure that the flow is completely developed.

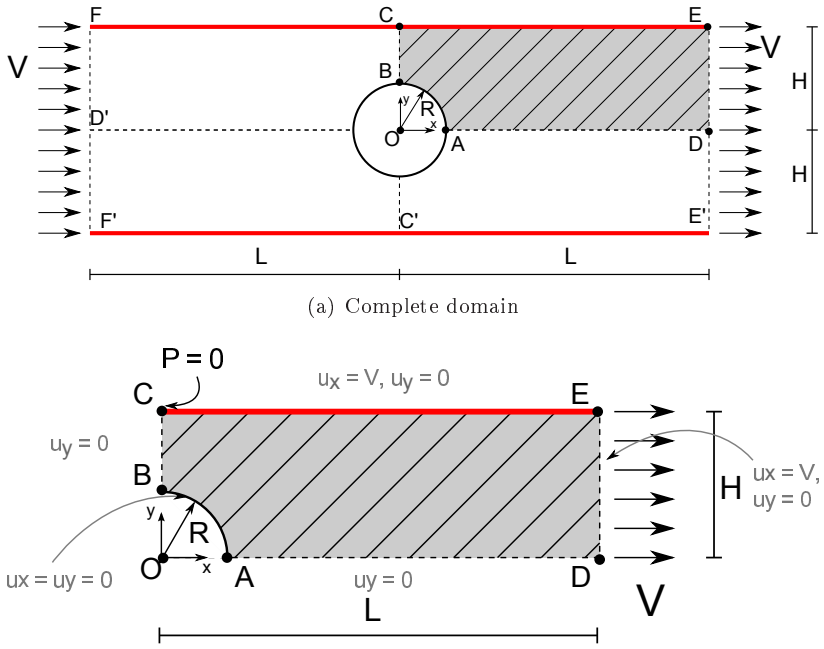

(a) Complete domain

(b) Reduced domain used in the analysis

Figure 8: Cylinder in a Bingham fluid. Geometry and boundary conditions

The properties of the material are summarized in Table 2. The Bingham number (Bn) in Table 2 is an adimensional quantity representing the ratio between the yield and the viscous stresses and it is calculated as $Bn = \tau_y(2R)/\mu_0 V$ where τ_y is the yield stress, H is the radius of the die, μ_0 is the plastic viscosity and V is the velocity of the fluid. A range of yield stresses (and, therefore, of Bingham numbers) is taken into account.

Different relations $H : R$ and $L : R$ have been considered to assess the effect of the domain size on the results. These are summarized in Table 3. In all the cases a more refined mesh is considered close to the cylinder (see Figure 9).

The results obtained in terms of yielded regions, drag force and stream lines are coherent with those obtained by [60]. In Figure 10 the yielded and unyielded regions are shown for different Bingham numbers for two different geometrical ratios $H : R = 4 : 1$ and $H : R = 10 : 1$. Figures 10(a) and 10(f) show the streamlines in the Newtonian case (i.e., $Bn = 0$). In the first case, the larger relative dimension of the

Material properties		
Plastic viscosity	μ_0	1 Pa· s
Yield stress	τ_y	0, 0.05, 0.5, 5, 50, 500 Pa
Bingham number	Bn	0, 0.1, 1, 10, 100, 1000
Regularization		
Regularization coefficient	m	1000 s

Table 2: Cylinder in a Bingham fluid. Material parameters and regularization coefficient

Mesh	**H : R**	**L : R**	**Nodes**	**Elements**
$M1$	2 : 1	12 : 1	783	1401
$M2$	4 : 1	24 : 1	3494	6623
$M3$	10 : 1	60 : 1	5371	10245
$M4$	50 : 1	250 : 1	13513	25473

Table 3: Cylinder in a Bingham fluid. Domains and meshes considered

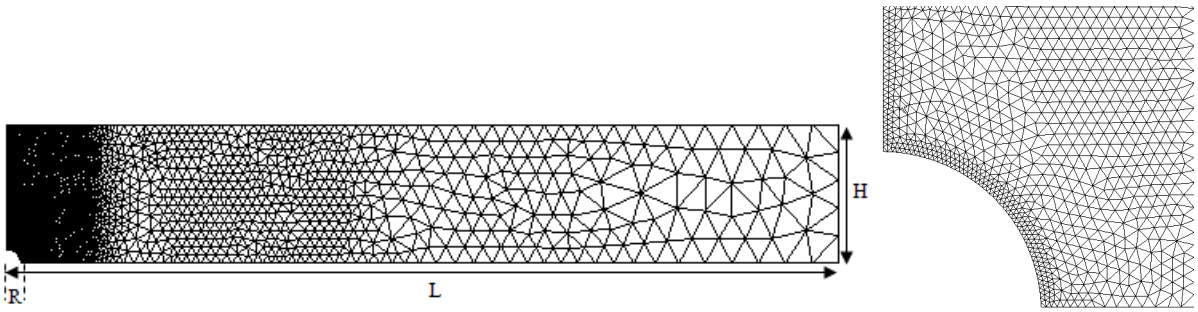

(a) Mesh of the whole domain (b) Mesh around the cylinder

Figure 9: Cylinder moving in a Bingham fluid. Unstructured mesh $M3$ with $H : R = 10$, $L : R = 60$

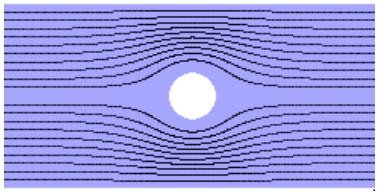

(a) $Bn = 0$, $H : R = 4 : 1$

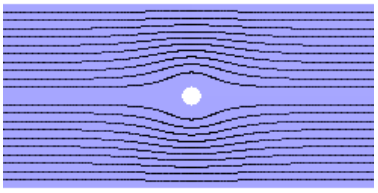

(f) $Bn = 0$, $H : R = 10 : 1$

(b) $Bn = 0.1$, $H : R = 4 : 1$

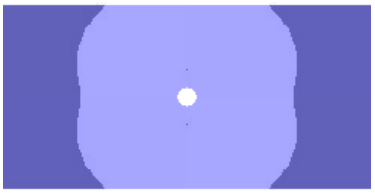

(g) $Bn = 0.1$, $H : R = 10 : 1$

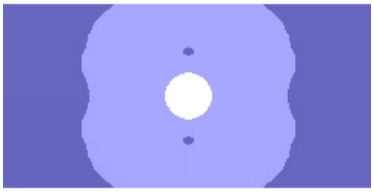

(c) $Bn = 1$, $H : R = 4 : 1$

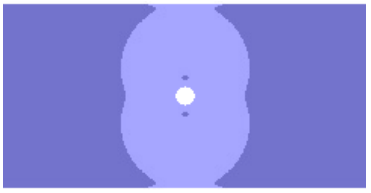

(h) $Bn = 1$, $H : R = 10 : 1$

(d) $Bn = 10$, $H : R = 4 : 1$

(i) $Bn = 10$, $H : R = 10 : 1$

(e) $Bn = 100s$, $H : R = 4 : 1$

(j) $Bn = 100s$, $H : R = 10 : 1$

Figure 10: Cylinder in a Bingham fluid. Stream lines and yielded (fair) and unyielded (dark) region for different Bingham numbers. On the left $H : R = 4 : 1$, on the right $H : R = 10 : 1$

cylinder leads to a steeper gradient of velocity in the y direction. For Bingham numbers $Bn > 10$, the drag force is independent from $H : R$. The yielded/unyielded regions, the recirculation and stagnation regions appear similarly to what happens in the case of a sphere. It is worth observing that as Bn increases:

- The yielded region around the cylinder decreases
- The unyielded region surrounds the cylinder. This process is more evident in the case $H : R = 10 : 1$, confirming that the wall effect in not negligible in the case $H : R = 4 : 1$.
- The recirculation islands immersed in the yielded region appear and get closer to the cylinder in a symmetric way. They finally adhere to the cylinder for $Bn = 100$.
- The stagnation zone appears at the side of the cylinder.
- The stagnation zone get smaller than the recirculation one.

The dimension and shape of the polar caps appearing in the stagnation regions is similar to the results presented in [8] and [86].

There is little information on the drag coefficient of a cylinder moving in a viscoplastic fluid. Roquet and Saramito [76] and Mitsoulis [60] present some studies on this specific problem. In Figure 11(a) the adimensional drag coefficient, Eq. (26), is plotted versus the Bingham number for the different cases analized and the results are compared with those of Mitsoulis showing a good agreement. It is worth observing that, as the Bingham number increases, the adimensional drag coefficient increases and becomes independent from the relation $H : R$ (for $H : R > 2$). When $Bn \to 0$, the adimensional drag reaches the value of the drag of a Newtonian fluid and when $Bn \to \infty$ it tends to $F_D^* = 1.14Bn$. This limit was also identified by Mitsoulis and Huigol [63]. The results obtained in this work are in the range of the limit values obtained by Adachi and Yoshioka [2] with their max and min theorem.

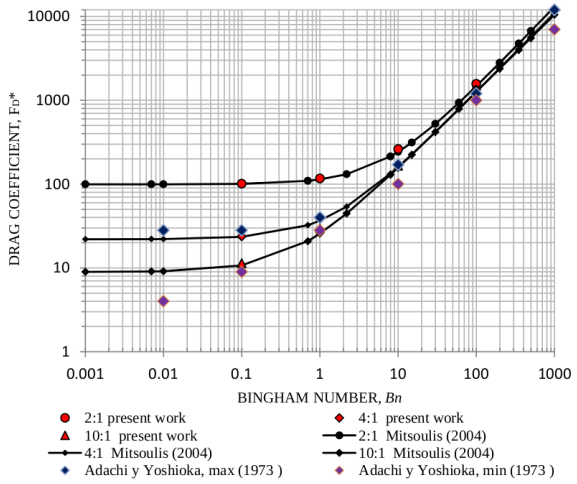

(a) Drag coefficient vs Bn

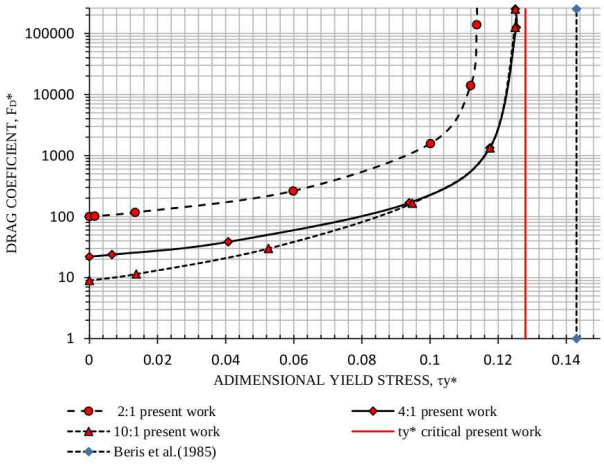

(b) Drag coefficient vs adimensional τ_y^*

Figure 11: Cylinder in a Bingham fluid. Drag coefficient. Comparison between the current work and other numerical solutions

Figure 11(b) shows that for high values of the adimensional yield stress the drag increases. The growth is progressively more steep as it gets to the critical limit of $\tau_y^* = 0.128$ (the red vertical line of Figure 11(b)). At this value of the yield stress, the drag force balances with the buoyancy force.

7 Numerical results: Herschel-Bulkley Fluids

7.1 Flow around a cylinder in an infinite medium

7.1.1 Description of the problem

The problem treated in this section is similar to the one presented in Section 6.2, but now the medium is infinite the flow follows the Herschel-Bulkley model. This is a complex and seldom studied phenomenon. In the literature there exist some studies on a sphere moving in a tube filled with a Herschel-Bulkley fluid at $Re \approx 0$ ([5], [6]). Some experimental results were provided by Atapattu [4] and, more recently, some experiments were performed on the flow around several spheres at low Re ($Re < 1$) confirming the difficulties on managing very low velocities ([57], [81]). Some authors have studied the movement of cylinders of different sizes inside a tube [62] and the flow around objects with different shapes with Re in the range $[10^{-1} - 10^{-8}]$ [48]. Mitsoulis provided a review of the results obtained for different problems on Bingham and Herschel-Bulkley flows [61] where the flow around a sphere in a viscoplastic medium is mentioned.

The flow around a cylinder in a Herschel-Bulkley pseudoplastic fluid in an infinite domain was studied by De Besses [38]. Tanner [82] presents numerical results for a cylinder moving in a pseudoplastic fluid (governed by a power law, without yield threshold) in an infinite domain. The problem in a confined domain was studied by [59] and [79]. Barthi et al. [9] included also dilatant fluids ($0.6 < n < 2$).

All the works mentioned are based on finite elements, except Bharti et al [9], where finite volumes were employed, and Tanner and Milthorpe [83], who used boundary elements. Sivakumar [79] compared finite elements and finite volumes results demonstrating the equivalence of both approaches.

The case of non-inertial flow of a Newtonian fluid around a cylinder in an infinite domain has no analytical solution; the reason being related to the shape of the streamlines far away from the cylinder, what is known as the Stoke's paradox [84]. The paradox does not present for pseudoplastic fluids ($n \leq 1$) and it is still unclear if it is present or not for dilatant flows ($n > 1$).

In the case of a flow in a finite domain the analytical solution does exist for all values of the flow index n ([28], [83]).

The objective of the current work is to study the flow around a cylinder in an infinite Herschel-Bulkley fluid domain. The determination of the drag force, the yielded and unyielded zones, as well as the recirculation and stagnation zones is carried out for different generalized Bingham numbers. The generalized Bingham number for an Herschel-Bulkley fluid is defined as $Bn^* = \frac{\tau_y}{k}\left(\frac{H}{V}\right)^n$.

Non inertial $Re \approx 0$ is assumed in all the examples.

7.1.2 Adimensional forces

The adimensional drag and lift coefficients in the specific case of a Herschel-Bulkley fluid are defined as

$$F_D^* = \frac{\frac{F_D}{Rl}}{k\left(\frac{V}{R}\right)^n} = \frac{F_D}{kR^{1-n}V^n l} \qquad ; \qquad F_L^* = \frac{\frac{F_L}{Rl}}{k\left(\frac{V}{R}\right)^n} = \frac{F_L}{kR^{1-n}V^n l} \tag{29}$$

where k is the consistency index of the fluid, V is the velocity of the cylinder and n is the flow index of the Herschel-Bulkley model.

7.1.3 Model and results

Figure 12 shows the geometry and boundary conditions used in the current example. The geometry is similar to that considered in Section 6.2, but in this case the semi-width of the domain, L, is taken sufficiently large not to influence the results. The minimum L for this is smaller for Bingham than for Newtoninan fluids and yet smaller for Herschel-Bulkley fluids.

The system of reference is fixed to the cylinder; therefore velocity boundary conditions are imposed on the external boundary of the domain (sides CE and ED in Figure 12). A no slip boundary condition is imposed on the surface of the cylinder. The radius of the cylinder is $R = 0.5$ m and the velocity in the x direction is $V = 1$ m/s Due to the double symmetry of the problem, just a quarter of the domain is simulated and symmetry conditions are imposed.

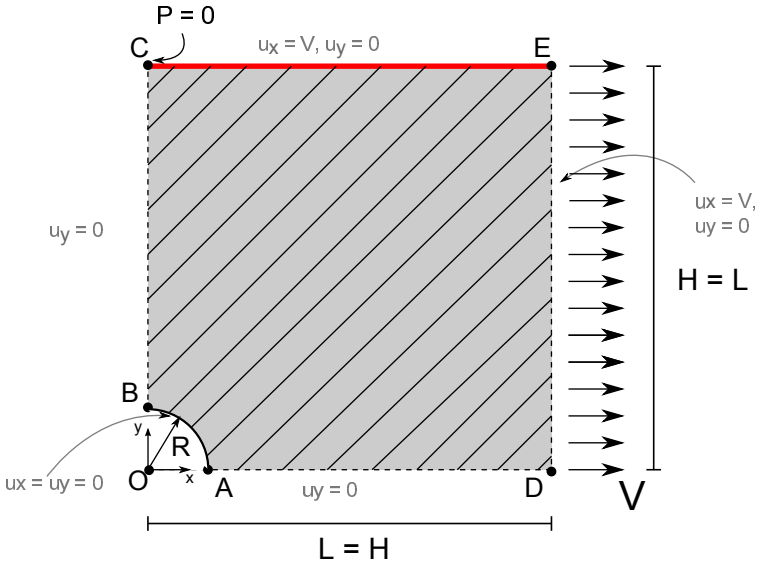

Figure 12: Cylinder in an Herschel-Bulkley fluid. Geometry and boundary conditions

Table 4 summarized the material properties of the model and the coefficients employed. Pseudoplastic ($n \leq 1$) and dilatant Herschel-Bulkley fluids are considered. The particular case of Bingham plastics ($n = 1$) is also taken into account. A regularization coefficient $m = 1000$ s is used in all the simulations.

Material properties		
y Yield stress	τ_y	1, 10, 100 Pa
Generalized Bingham Number Bn^*		1, 10, 100
Flow index	n	0.25, 0.5, 0.75, 1, 2
Regularization		
Regularization coefficient	m	1000 s

Table 4: Cylinder in an Herschel-Bulkley fluid. Material parameters and regularization coefficient

It can be observed in Figure 14 that the adimensional drag coefficient (F_D^*) grows with the flow index n, independently from the geometrical ratio, for $L : R \geq 50 : 0.5$. This means that it is sufficient to consider a domain with that minimum geometrical ratio to ensure insensitivity of the flow from the artificial domain boundaries. It is evident form the results that the drag coefficient is linearly related to the flow index n for $n \geq 0.5$.

The case of a pseudoplastic Herschel-Bulkley fluid is studied first. Figures 15(a) and 15(b) present the adimensional drag, F_D^*, and the drag force over the yield stress, $F_D^{'} = F_D/\tau_y$, respectively, versus the

Mesh	L : R	Nodes	Elements
$M1$	100 : 0.5	9367	18351
$M2$	500 : 0.5	9500	18601
$M3$	1000 : 0.5	9571	18729

Table 5: Cylinder in an Herschel-Bulkley fluid. Domains and meshes considered

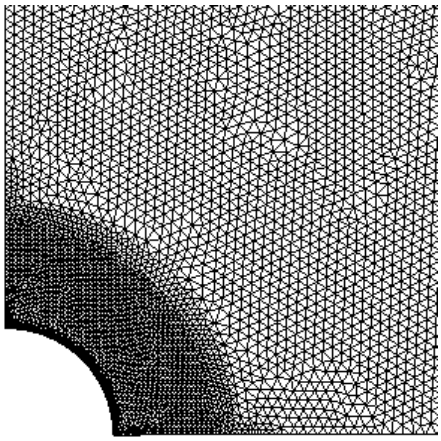

Figure 13: Cylinder in an Herschel-Bulkley fluid. Unstructured mesh

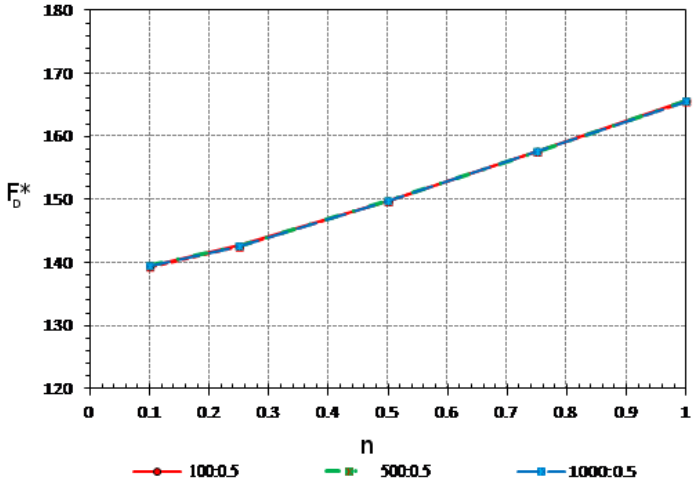

Figure 14: Cylinder in an Herschel-Bulkley fluid. Drag force coefficient in terms of the relation $L : R$

generalized Bingham number ($Bn^* = 0.1$, 1, 10, 100), for different flow indexes ($n = 0.25$, 0.5, 0.75, 1). The drag coefficient grows as Bn^* increases (Figure 15(a)) and the yield stress effect is higher for higher values of Bn^* (Figure 15(b)).

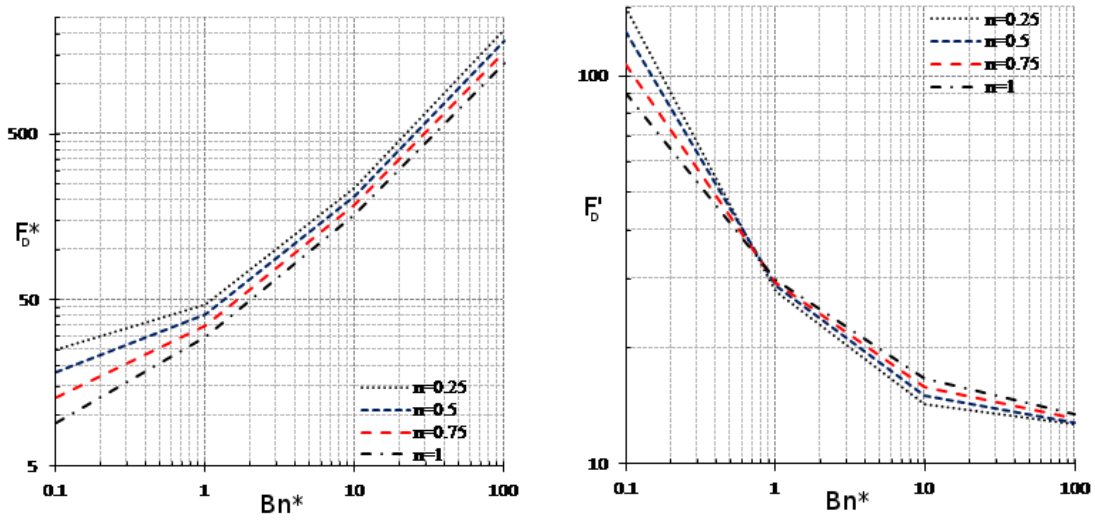

(a) Drag force vs Bn

(b) Drag coefficient related to the yield stress

Figure 15: Cylinder in an Herschel-Bulkley fluid. Drag force and Drag coefficient for different flow indexes n

The differences in the yielded and unyielded regions for different generalized Bingham numbers Bn^* are evident in Figure 16 where the yielded region is plotted in grey for a $Bn^* = 10$ (Figure 16(a)) and for a $Bn^* = 100$ (Figure 16(b)). The increment of the Bn^* induces a shape and volumetric change of the yielded region which reduces significantly especially in the direction of the flow.

The stagnation and recirculation regions in terms of Bn^* and n are shown in Figure 17. The stagnation regions are very sensitive to the Bn^* while being almost insensitive to the value of the flow index n. In the stagnation region triangular shaped polar caps, similar to those obtained studying the falling of a sphere in [8], can be observed.

The recirculation zone on the y axis increases when Bn^* or n increase. The yielded thin layer between these regions and the cylinder reduces for higher values of Bn^*, and increases with n. The no slip condition on the cylinder does not allow this "boundary layer" to disappear even for very high values of Bn^*. The effect of an alternative slip boundary condition on the cylinder can be found in [38]. While the recirculation regions obtained match very well with those obtained by De Bresse in [38], the polar caps are significantly smaller. This is the consequence of the OSS stabilization technique used, that allows to solve with a high level of detail these critical parts of the domain.

The case of a dilatant Herschel-Bulkley fluid is considered next. The flow index is taken $n = 2$. The magnitude of the velocity field is smaller in the dilatant case than in the pseudoplastic one. As shown in Figure 18, the yielded region has the shape of two circles intersected along the x axis and it reduces when Bn^* increases much more faster than in the pseudoplastic case.

The polar caps start to be visible for $Bn^* \geq 1$ while the recirculation regions are always present. These are bigger and more separated from the cylinder than in the corresponding pseudoplastic case (Figure 19).

The drag coefficient in the dilatant case follows a similar dependency with Bn^* and τ_y as in the pseudoplastic case, but its absolute value is much lower.

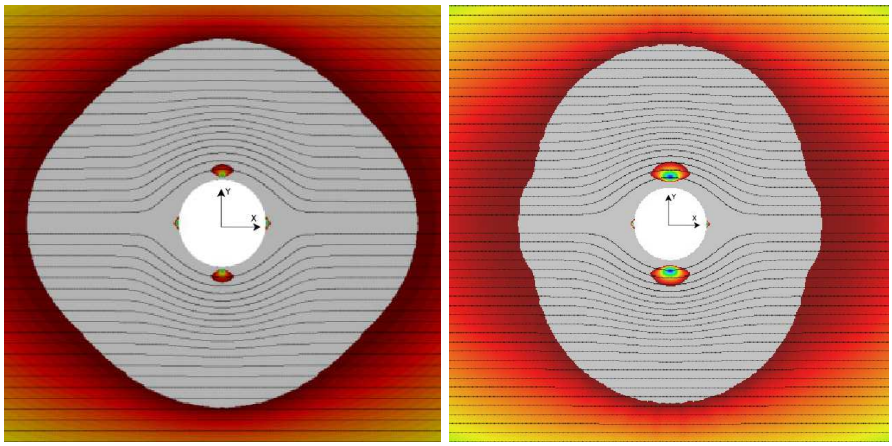

(a) $Bn^* = 10$ (b) $Bn^* = 100$

Figure 16: Cylinder in an Herschel-Bulkley fluid. Yielded (grey) and unyielded (coloured) regions and flow streamlines. Recirculation zones on y axis and stagnation zones (with polar caps) on x axis

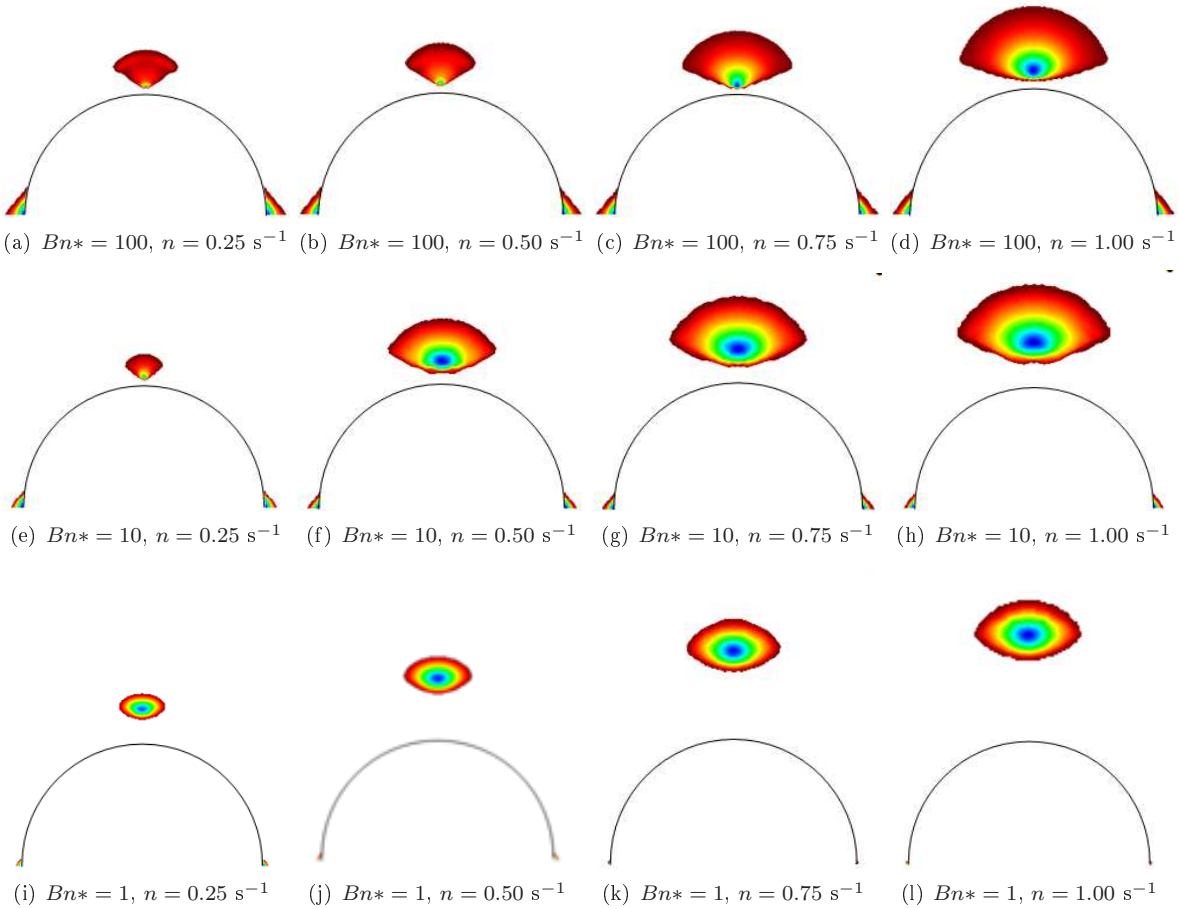

(a) $Bn* = 100$, $n = 0.25$ s^{-1} (b) $Bn* = 100$, $n = 0.50$ s^{-1} (c) $Bn* = 100$, $n = 0.75$ s^{-1} (d) $Bn* = 100$, $n = 1.00$ s^{-1}

(e) $Bn* = 10$, $n = 0.25$ s^{-1} (f) $Bn* = 10$, $n = 0.50$ s^{-1} (g) $Bn* = 10$, $n = 0.75$ s^{-1} (h) $Bn* = 10$, $n = 1.00$ s^{-1}

(i) $Bn* = 1$, $n = 0.25$ s^{-1} (j) $Bn* = 1$, $n = 0.50$ s^{-1} (k) $Bn* = 1$, $n = 0.75$ s^{-1} (l) $Bn* = 1$, $n = 1.00$ s^{-1}

Figure 17: Cylinder in an Herschel-Bulkley fluid. Dependency of the unyielded regions in terms of the Bingham number and the flow index

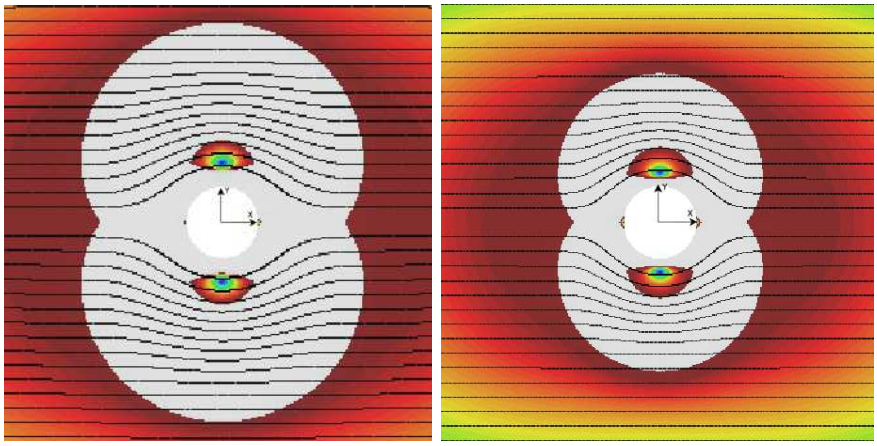

(a) $Bn^* = 10$ (b) $Bn^* = 100$

Figure 18: Cylinder in a dilatant Herschel-Bulkley fluid ($n = 2$). Yielded (grey) and unyielded (coloured) regions and flow streamlines. Recirculation region on y axis and stagnation zone (with polar caps) on x axis

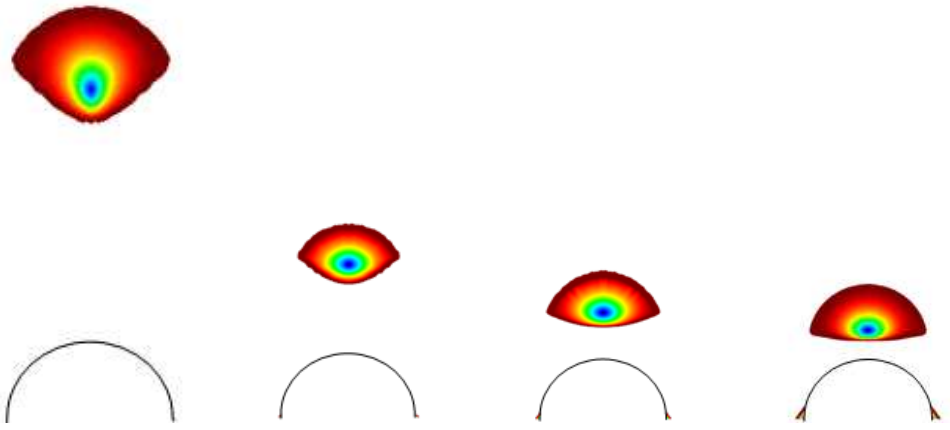

(a) $Bn^* = 0.1$ (b) $Bn^* = 1$ (c) $Bn^* = 10$ (d) $Bn^* = 100$

Figure 19: Cylinder in a dilatant Herschel-Bulkley fluid ($n = 2$). Growth of the unyielded regions in terms of Bn^*

The shape of the stagnation and the recirculation regions are in good accordance with those obtained in [8] and [2] also, although in the latter the shape of the zones was more rounded.

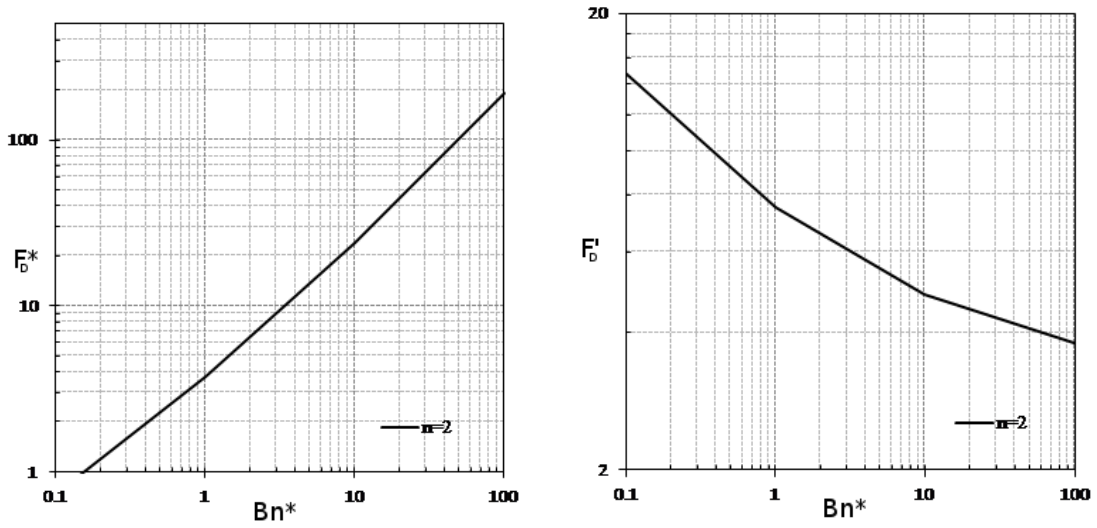

(a) Drag coefficient

(b) Drag coefficient related to the yield stress

Figure 20: Cylinder in a dilatant Herschel-Bulkley fluid $n = 2$. Drag coefficient versus the Bingham number Bn^* and the yield stress

7.2 Flow around a moving cylinder rotating around its axis

7.2.1 Description of the problem

The last example simulates a rotating cylinder moving between parallel planes in a Herschel-Bulkley fluid.

The principal objective is to study the yielded and unyielded region, to define the localization pattern of the strain rate and to see the evolution of the stream lines at different velocities of rotation.

7.2.2 Model and results

The geometrical setting is similar to the one described in Section 6.2, but with the cylinder rotating around its axis. The problem is therefore antisymmetric with respect to the vertical axis y (Figure 21). This implies that only half of the domain needs to be simulated (the shaded area in Figure 21), provided suitable boundary conditions are imposed on the plane of antisymmetry. The reference system is moving with the cylinder; therefore, on the outer boundary of the domain $u_x = V = 1$ m/s is imposed in the x direction, while $u_y = 0$ m/s. A no slip boundary condition is imposed on the surface of the cylinder.

Table 6 summarizes the properties of the material and the regularization parameter used. The flow index of the Harshel-Bulkley model is $n = 0.25$, which corresponds to a highly pseudoplastic fluid.

The aspect ratio of the computational domain is $H : R = 10 : 1$ and $L : R = 30 : 1$. The unstructured mesh used in the example is shown in Figure 22(a); it is composed of 9425 nodes and 18345 linear triangular elements. The average size of the elements on the surface of the cylinder (see Figure 22(b)) is of 0.01 m, whereas on the vertical line (from B to C and from G to C' in Figure 21) the element size varies from 0.01 m to 0.04 m.

Material properties		
Consistency index	k	1 Pa· s^n
Yield stress	τ_y	100 Pa
Flow index	n	0.25
Regularization		
Regularization coefficient m		1000 s

Table 6: Moving and rotating cylinder in an Herschel-Bulkley fluid. Material parameters and regularization coefficient

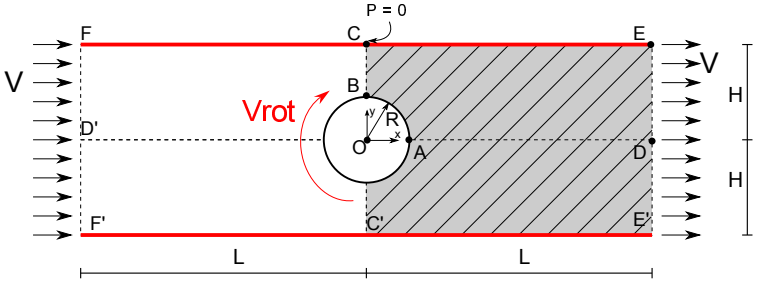

Figure 21: Moving and rotating cylinder in an Herschel-Bulkley fluid. Geometry and boundary conditions

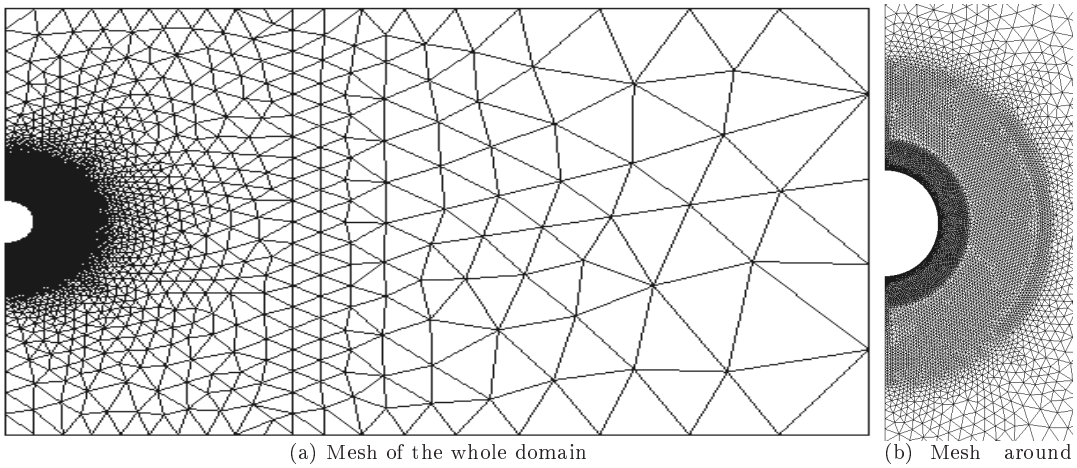

(a) Mesh of the whole domain

(b) Mesh around the cylinder

Figure 22: Moving and rotating cylinder in an Herschel-Bulkley fluid. Unstructured mesh used for the calculation

Four different velocities of rotation (V_{ROT}) have been studied: 0, 0.5, 1.0 and 5 m/s. The symmetry with respect to the x axis observed for $V_{ROT} = 0$ m/s (Figure 23(a)) is lost when the cylinder starts rotating. Under these circumstances only symmetry with respect to the vertical axis y is maintained (Figures 23(b)-23(d)). This is confirmed by the streamlines (Figures 24(a)-24(d)).

The increment of the velocity of rotation makes one of the slip lines progressively disappear while the other moves closer to the cylinder. On one side of the cylinder the rotational velocity adds to the linear velocity, while it is opposed on the opposite side. For high values of the rotational velocity (Figure 23(d)) the rate of strain localization concentrates around the cylinder.

The slip lines of Figure 23 correspond to the change of slope in the streamlines (Figure 24) that reduces their relative distance.

Figures 24(a)-24(d) show the complex evolution of the yielded and unyielded regions as the velocity of rotation increases. The recirculation zone increases arriving to define a semi circle for $V_{ROT} = 1$ m/s and it disappears for $V_{ROT} = 5$ m/s, leaving a thin layer of unyielded material close to the surface while the size of the recirculation region under the cylinder increases. The growth of the stagnation region culminates for $V_{ROT} = 1$ m/s and no polar caps are present for higher velocities.

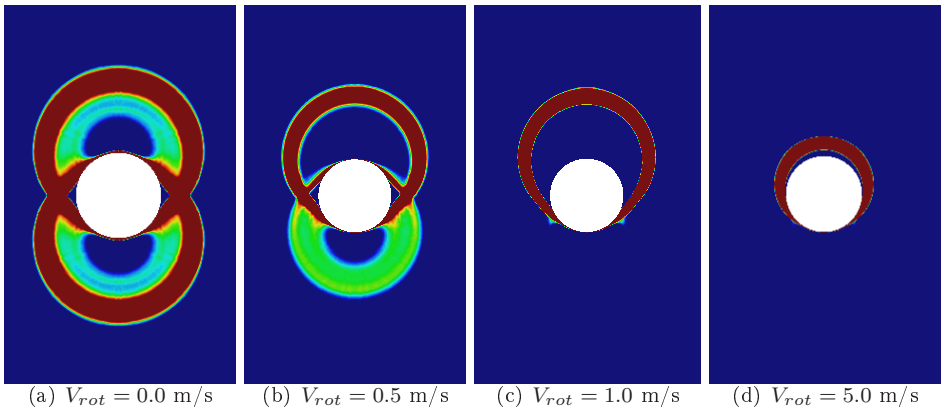

(a) $V_{rot} = 0.0$ m/s (b) $V_{rot} = 0.5$ m/s (c) $V_{rot} = 1.0$ m/s (d) $V_{rot} = 5.0$ m/s

Figure 23: Moving and rotating cylinder in an Herschel-Bulkley fluid. Localization of strain rate for different rotational velocities

The drag decreases as the velocity of rotation increases. On the contrary, the lift coefficient, which is null when the cylinder is not rotating, increases with the velocity of rotation. It is worth noting that the drag is substantially higher than the lift in all the cases.

8 Conclusions

In the present work a mixed stabilized finite element formulation for Bingham and Herschel-Bulkley fluids is presented. The implementation of an OSS stabilization technique allows to use equal order interpolation of velocity and pressure (i.e., $P1/P1$ linear elements), avoiding both the pressure and velocity oscillations and leading to a stable and accurate solution.

On the one hand, being OSS a residual based stabilization technique, no consistency error is introduced. On the other hand, constructing the subscale in the subspace orthogonal to the finite element one leads to a minimization of the numerical dissipation on the discrete solution.

The extrusion process of a Bingham fluid with the section reduced by 2/3 shows a correct definition of the slip lines according to Pradtl's theory. A cylinder moving between two parallel planes is the second example studied. The comparison with the results obtained by other authors leads to the conclusion that the presented technique reproduces correctly the yielded and unyielded regions, as well as calculates the correct drag for different Bingham numbers and geometrical relations. Pseudoplastic and dilatant cases of

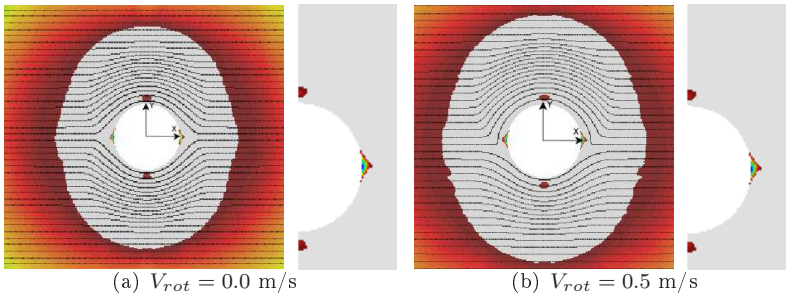

(a) $V_{rot} = 0.0$ m/s (b) $V_{rot} = 0.5$ m/s

(c) $V_{rot} = 1.0$ m/s (d) $V_{rot} = 5.0$ m/s

Figure 24: Moving and rotating cylinder in an Herschel-Bulkley fluid. Streamlines and yielded and unielded regions for different rotational velocities

Herschel-Bulkley are are also used to study a cylinder moving in an infinite domain and a cylinder moving and rotating around its axis. Also in these cases, the polar caps and recirculation regions are correctly reproduced.

Acknowledgements

The research was supported by the Spanish Ministry of Economy and Competitiveness (*Ministerio de Economía y Competitividad*, MINECO) through the project EACY (MAT2013-48624-C2-1-P). The financial support of the ERC Advanced Grant project SAFECON (AdG-267521) of the European Research Council and of the T-MAPPP project (FP7 PEOPLE 2013 ITN-G.A.n607453) is also greatly acknowledged.

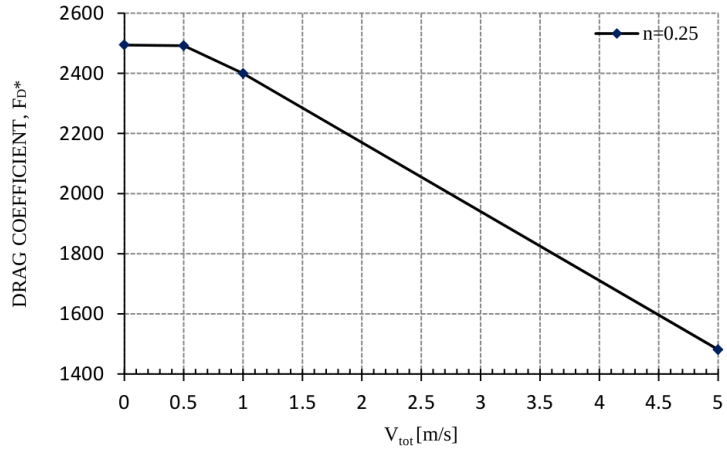

(a) Drag coefficient

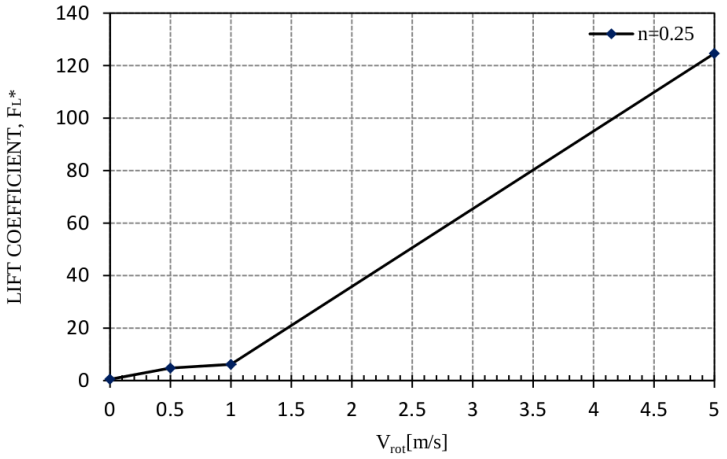

(b) Lift coefficient

Figure 25: Moving and rotating cylinder in an Herschel-Bulkley fluid $n = 0.25$. Drag and lift for different rotational velocities

References

[1] S.S. Abdali, E. Mitsoulis, and N.C. Markatos. Entry and exit flows of bingham fluids. *Journal of Rheology*, 36(2):389 – 407, 1992.

[2] K. Adachi and N. Yoshioka. On creeping flow of a visco-plastic fluid past a circular cylinder. *Chemical Engineering Science*, 28(1):215–226, 1973.

[3] J.M. Alexander. On complete solution for frictionless extrusion in plane strain. *Quart. Appl. Math*, 19:31 – 40, 1961.

[4] D. D. Atapattu, R. P. Chhabra, and P. H. T. Uhlherr. Creeping sphere motion in herschel-bulkley fluids: flow field and drag. *Journal of non-newtonian fluid mechanics*, 59(2):245–265, 1995.

[5] D.D. Atapattu, R.P. Chhabra, and P.H.T. Uhlherr. Wall effect for spheres falling at small reynolds number in a viscoplastic medium. *Journal of Non-Newtonian Fluid Mechanics*, 38(1):31 – 42, 1990.

[6] M. Beaulne and E. Mitsoulis. Creeping motion of a sphere in tubes filled with herschel-bulkley fluids. *Journal of non-newtonian fluid mechanics*, 72(1):55–71, 1997.

[7] M. Bercovier and M. Engelman. A finite-element method for incompressible non-newtonian flows. *Journal of Computational Physics*, 36(3):313 – 326, 1980.

[8] A.N. Beris, J.A. Tsamopoulos, R.C. Armstrong, and R.A. Brown. Creeping motion of a sphere though a bingham plastic. *Journal of Fluid Mechanics*, 158:219–244, 1985.

[9] R. P. Bharti, R. P. Chhabra, and V. Eswaran. Steady flow of power law fluids across a circular cylinder. *The Canadian Journal of Chemical Engineering*, 84(4):406–421, 2006.

[10] E. Bingham. *Fluidity and Plasticity*. McGraw-Hill, New York, 1922.

[11] R. Bird, R. Armstrong, and O. Hassager. *Dynamics of Polymeric Liquids, Volume 1, Fluid Mechanics, 2nd Edition*. John Wiley and Sons, New Yok, 1987.

[12] R.B. Bird. *Dynamics of polymeric liquids*. John Wiley and Sons, 1987.

[13] J. Blackery and E. Mitsoulis. Creeping motion of a sphere in tubes filled with a bingham plastic material. *Journal of Non-Newtonian Fluid Mechanics*, 70(1-2):59 – 77, 1997.

[14] F. Brezzi and M. Fortin. *Mixed and Hybrid Finite Element Methods*. Springer-Verlag, Berlin/New York, 1991.

[15] A.N. Brooks and T.J.R. Hughes. Streamline upwind/petrov-galerkin formulations for convection dominated flows with particular emphasis on the incompressible navier-stokes equations. *Computer Methods in Applied Mechanics and Engineering*, 32(1Ũ3):199 – 259, 1982.

[16] E. Castillo and R. Codina. Stabilized stress-velocity-pressure-finite element formulations of the navier-stokes problem for fluids with non-linear viscosity. *Computer Methods in Applied Mechanics and Engineering*, 279:554–578, 2014.

[17] E. Castillo and R. Codina. Variational multi-scale stabilized formulations for the stationary three-field incompressible viscoelastic flow problem. *Computer Methods in Applied Mechanics and Engineering*, 279:579–605, 2014.

[18] M. Cervera and M. Chiumenti. Size effect and localization in j2 plasticity. *International Journal of Solids and Structures*, 46(17):3301 – 3312, 2009.

[19] M. Cervera, M. Chiumenti, and R. Codina. Mixed stabilized finite element methods in nonlinear solid mechanics. part i: Formulation. *Computer Methods in Applied Mechanics and Engineering*, 199:2559 – 2570, 2010.

[20] M. Cervera, M. Chiumenti, and R. Codina. Mesh objective modeling of cracks using continuous linear strain and displacement interpolations. *International Journal for Numerical Methods in Engineering*, 87(10):962 – 987, 2011.

[21] M. Cervera, M. Chiumenti, and C. Angelet de Saracibar. Shear band localization via local j2 continuum damage mechanics. *Computer Methods in Applied Mechanics and Engineering*, 193:849–880, 2004.

[22] M. Cervera, M. Chiumenti, and C.A. de Saracibar. Softening, localization and stabilization: Capture of discontinuous solutions in j2 plasticity. *International Journal for Numerical and Analytical Methods in Geomechanics*, 28(5):373 – 393, 2004.

[23] M. Cervera, M. Chiumenti, and Q. Valverde C. Agelet de Saracibar. Mixed linear/linear simplicial elements for incompressible elasticity and plasticity. *Computer Methods in Applied Machanics and Engineering*, 192:5249–5263, 2003.

[24] R .P. Chhabra. *Bubbles, Drops, and Particles in Non-Newtonian Fluids, Second Edition. Print ISBN: 978-0-8247-2329-3 eBook ISBN: 978-1-4200-1538-6.* CRC press Balkema, 2006.

[25] R. P. Chhabra, K. Rami, and P. H. T. Uhlherr. Drag on cylinders in shear thinning viscoelastic liquids. *Chemical engineering science*, 56(6):2221–2227, 2001.

[26] R.P. Chhabra. *Encyclopedia of fluid mechanics,*, chapter Steady non-Newtonian flow about a rigid sphere, pages 983–1033. Gulf, Houston, 1986.

[27] R.P. Chhabra. *Non-Newtonian Fluids: An Introduction, Rheology of Complex Fluids (Chapter 1).* Springer, 2010.

[28] R.P. Chhabra and J.F. Richardson. *Non-newtonian flow and applied rheology.* Engineering applications, 2008.

[29] M. Chiumenti, M. Cervera, and R. Codina. A mixed three-field fe formulation for stress accurate analysis including the incompressible limit. *Computer Methods in Applied Mechanics and Engineering*, 283:1095 – 1116, 2015.

[30] M. Chiumenti, Q. Valverde, C. Agelet De Saracibar, and M. Cervera. A stabilized formulation for incompressible elasticity using linear displacement and pressure interpolations. *Computer Methods in Applied Mechanics and Engineering*, 191(46):5253 – 5264, 2002.

[31] R. Codina. Comparison of some finite element methods for solving the diffusion-convection-reaction equation. *Computer Methods in Applied Mechanics and Engineering*, 156(1-4):185 – 210, 1998.

[32] R. Codina. On stabilized finite element methods for linear system of convection-diffusion-reaction equations. *Computer Methods in Applied Machanics and Engineering*, 188:61–82, 2000.

[33] R. Codina. Stabilization of incompressibility and convection through orthogonal sub-scales in finite element method. *Computer Methods in Applied Machanics and Engineering*, 190:1579–1599, 2000.

[34] R. Codina. Stabilized finite element approximation of transient incompressible flows using orthogonal subscales. *Computer Methods in Applied Mechanics and Engineering*, 191:4295–4321, 2002.

[35] R. Codina and O. Soto. Approximation of the incompressible navier-stokes equations using orthogonal subscale stabilization and pressure segregation on anisotropic finite element meshes. *Computer Methods in Applied Machanics and Engineering*, 193:1403–1419, 2004.

[36] A.H. Coppola and R. Codina. Improving eulerian two-phase flow finite element approximation with discontinuous gradient pressure shape functions. *Int. J. Numer. Meth. Fluids*, 49:1287.1304, 2005.

[37] P. Coussot. Yield stress fluid flows: a review of experimental data. *Journal of Non-Newtonian Fluid Mechanics*, 211:31–49, 2014.

[38] B. D. De Besses, A. Magnin, and P. Jay. Viscoplastic flow around a cylinder in an infinite medium. *Journal of non-newtonian fluid mechanics*, 115(1):27–49, 2003.

[39] M. Diez and L. Godoy. Flujo viscoplástico incompresible de materiales con fricción y cohesión. aplicación a problemas bidimensionales. *Revista Internacional de Métodos Numéricos para Cálculo en Ingeniería*, 7 (4):417 – 436, 1991.

[40] D.D. dos Santos, S. Frey, M.F. Naccache, and P.R. de Souza Mendes. Numerical approximations for flow of viscoplastic fluids in a lid-driven cavity. *Journal of Non-Newtonian Fluid Mechanics*, 166(12-13):667 – 679, 2011.

[41] P. T. Griffiths. Flow of a generalised newtonian fluid due to a rotating disk. *Journal of Non-Newtonian Fluid Mechanics*, 221:9–17, 2015.

[42] F. Händle. *Extrusion in Ceramic*. Springer, Berlin, 2007.

[43] W. Herschel and R. Bulkley. Measurement of consistency as applied to rubber-benzene solutions. *Proceeding of American Society of Testing Material*, 26:621–633, 1926.

[44] R. Hill. A theoretical analysis of the stresses and strains in extrusionand piercing. *Journal Iron Steel Institute,*, 159:177–185, 1948.

[45] T.J.R. Hughes. Multiscale phenomena: Green's function, the dirichlet to neumann formulation, subgrid scale models, bubbles and the origins of stabilized formulations. *Computer Methods in Applied Machanics and Engineering*, 127:387–401, 1995.

[46] T.J.R. Hughes, G.R. Feijóo, L. Mazzei, and J.-B. Quincy. The variational multiscale method - a paradigm for computational mechanics. *Computer Methods in Applied Mechanics and Engineering*, 166(1-2):3–24, 1998.

[47] T.J.R. Hughes, L.P. Franca, and G.M. Hulbert. A new finite element formulation for computational fluid dynamics: Viii. the galerkin/least-squares method for advective-diffusive equations. *Computer Methods in Applied Mechanics and Engineering*, 73(2):173–189, 1989.

[48] L. Jossic and A. Magnin. Drag and stability of objects in a yield stress fluid. *AIChE journal*, 47(12):2666–2672, 2001.

[49] A. Larese, E. Oñate, and R. Rossi. *A coupled Eulerian-PFEM model for the simulation of overtopping in rockfill dams. ISBN: 978-84-940243-6-8, Deposito legal: B-29348-2012.1.* Monograph CIMNE M133, 2012.

[50] A. Larese, R. Rossi, E.Oñate, and M.A. Toledo. Physical and numerical modelization of the behavior of rockfill dams during overtopping scenarios. *Dam Maintenance and Rehabilitation II. CRCpress Balkema. ISBN:978-0-415-61648-5*, pages 479–487, 2010.

[51] A. Larese, R. Rossi, E. Oñate, and S.R. Idelsohn. A coupled pfem- eulerian approach for the solution of porous fsi problems. *Computational Mechanics, DOI: 10.1007/s00466-012-0768-9*, 50 (6):805–819, 2012.

[52] A. Larese, R. Rossi, and E. Oñate. Finite element modeling of free surface flow in variable porosity media. *Archives for Numerical Methods in Engineering DOI: 10.1007/s11831-014-9140-x*, 2014.

[53] E. Lee. *Numerical analysis of forming processes*, chapter Finite deformation effects in plasticity analysis, pages 373 – 386. Jhon Wiley and Sons. Chichester, U. K, 1984.

[54] B. T. Liu, S. J. Muller, and M. M. Denn. Convergence of a regularization method for creeping flow of a bingham material about a rigid sphere. *Journal of non-newtonian fluid mechanics*, 102(2):179–191, 2002.

[55] J. Lubliner. *Plasticity Theory*. Macmillan Publishing Company, New York, NY., 1990.

[56] J. Mandel. Ondes platiques dans un mileu indéfini á trois dimensions. *Journal de Mécanique*, 1:3 – 30, 1962.

[57] O. Merkak, L. Jossic, and A. Magnin. Spheres and interactions between spheres moving at very low velocities in a yield stress fluid. *Journal of non-newtonian fluid mechanics*, 133(2):99–108, 2006.

[58] L. Minatti and A. Pasculli. Sph numerical approach in modelling 2d muddy debris flow. *International Conference on Debris-Flow Hazards Mitigation: Mechanics, Prediction, and Assessment*, pages pp. 467–475, 2011.

[59] K. A. Missirlis, D. Assimacopoulos, E. Mitsoulis, and R. P. Chhabra. Wall effects for motion of spheres in power-law fluids. *Journal of non-newtonian fluid mechanics*, 96(3):459–471, 2001.

[60] E. Mitsoulis. On creeping drag flow of a viscoplastic fluid past a circular cylinder: wall effects. *Chemical engineering science*, 59(4):789–800, 2004.

[61] E. Mitsoulis. Annular extrudate swell of pseudoplastic and viscoplastic fluids. *Journal of non-newtonian fluid mechanics*, 141(2):138–147, 2007.

[62] E. Mitsoulis and S. Galazoulas. Simulation of viscoplastic flow past cylinders in tubes. *Journal of Non-Newtonian Fluid Mechanics*, 158(1):132–141, 2009.

[63] E. Mitsoulis and R.R. Huilgol. Entry flows of bingham plastics in expansions. *Journal of Non-Newtonian Fluid Mechanics*, 122(1-3):45 – 54, 2004.

[64] E. Mitsoulis and Th. Zisis. Flow of bingham plastics in a lid-driven square cavity. *Journal of Non-Newtonian Fluid Mechanics*, 101:173 – 180, 2001.

[65] J. G. Oldroyd. A rational formulation of the equations of plastic flow for a bingham solid. *Mathematical Proceedings of the Cambridge Philosophical Society*, 43:100 – 105, 1 1947.

[66] E. Oñate. La formulación del flujo viscoplástico y sus diversas aplicaciones prácticas por el método de los elementos finitos. *Revista de Obras Públicas*, 127 (3178):115 – 129, 1980.

[67] T. C. Papanastasiou. Flows of materials with yield. *Journal of Rheology*, 31:385 – 404, 1987.

[68] D. Perić and S. Slijepcević. Computational modelling of viscoplastic fluids based on a stabilised finite element method. *Engineering Computations*, 18:577 – 591, 2001.

[69] J. M. Piau. Viscoplastic boundary layer. *Journal of non-newtonian fluid mechanics*, 102(2):193–218, 2002.

[70] R. Planas, S. Badia, and R. Codina. Aproximation of the inductionless mhd problem using a stabilized finite element method. *Journal of Computational Physics*, 230:2977 – 2966, 2011.

[71] W. Prager. *Introduction to mechanics of continua*. Dover, New York, 1973.

[72] L. Prandtl. Uber dire harte plastischer korper. *Gottinger Nachrichten*, pages 74–85, 1920.

[73] A. M. V. Putz, T. I. Burghelea, I. A. Frigaard, and D. M. Martinez. Settling of an isolated spherical particle in a yield stress shear thinning fluid. *Physics of Fluids*, 20(3), 2008.

[74] E. Reiner. *Handbuch der Phisik*. Springer, Berlin, 1958.

[75] A. Remaitre, J. P. Malet, O. Maquaire, C. Ancey, and J. Locat. Flow behaviour and runout modelling of a complex debris flow in a clay-shale basin. *Earth surface processes and landforms*, 30 (4):479–488, 2005.

[76] N. Roquet and P. Saramito. An adaptive finite element method for bingham fluid flows around a cylinder. *Computer methods in applied mechanics and engineering*, 192(31):3317–3341, 2003.

[77] R. Rossi, A. Larese, P. Dadvand, and E: Oñate. An efficient edge-based level set finite element method for free surface flow problems. *International Journal for Numerical Methods in Fluids, DOI: 10.1002/fld.3680*, 71 (6):687–716, 2013.

[78] F. Salazar, J. Irazabal, A. Larese, and E. Oñate. Numerical modelling of landslide-generated waves with the particle finite element method (pfem) and a non-newtonian flow model. *Submitted to the International Journal for Numerical and Analytical Methods in Geomechanics*, 2015.

[79] P. Sivakumar, R.P. Bharti, and R.P. Chhabra. Effect of power-law index on critical parameters for power-law flow across an unconfined circular cylinder. *Chemical Engineering Science*, 61(18):6035 – 6046, 2006.

[80] S. Slijepcević and D. Perić. Some aspects of computational modelling of non-newtonian fluids based on a stabilised finite element method. 2004.

[81] H. Tabuteau, P. Coussot, and J.R. De Bruyn. Drag force on a sphere in steady motion through a yield-stress fluid. *Journal of Rheology*, 51(1):125 – 137, 2007.

[82] R. I. Tanner. Stokes paradox for power-law flow around a cylinder. *Journal of non-newtonian fluid mechanics*, 50(2):217–224, 1993.

[83] R.I. Tanner and J.F. Milthorpe. Numerical simulation of the flow of fluids with yield stresses. pages 680 – 690, 1983.

[84] M. Van Dyke. *Perturbation methods in fluid mechanics (Vol. 964)*. New York: Academic Press, 1964.

[85] K. Walters and R. I. Tanner. *The motion of a sphere through an elastic fluid. Transport Processes in Bubbles, Drops, and Particles*. Hemisphere, New York, NY, 1992.

[86] N. Yoshioka and K. Adachi. On variational principles for a non-newtonian fluid. *Journal of Chemical Engineering of Japan*, 4(3):217–220, 1971.

[87] O. Zienkiewicz, P. Jain, and E. Oñate. Flow of solids diuring forming and extrusion: some aspects of numerical solutions. *International Journal of Solids and Structures*, 14:15–38, 1978.

[88] T. Zisis and E. Mitsoulis. Viscoplastic flow around a cylinder kept between parallel plate. *Journal of non-newtonian fluid mechanics*, 105(1):1–20, 2002.